#295

LEVEL II

2

AD A100151

DTIC ELECTE JUN 1 2 1981 S C D

6 THE QUALIFICATION OF TARGET MATERIALS USING THE INTEGRAL THEORY OF IMPACT.

10 C. duP. /Donaldson Ross M. /Contiliano
Claude 1. /Swanson

14 ARAP-295

AERONAUTICAL RESEARCH ASSOCIATES OF PRINCETON, INC.
50 WASHINGTON ROAD, PRINCETON, NEW JERSEY 08540

15 DAAD05-76-C-0757

12 71

11 DEC[redacted]976

9 INTERIM REPORT [redacted] 15 MAR[redacted] 15 DEC[redacted]76,

DISTRIBUTION STATEMENT A

Approved for public release;
Distribution Unlimited

PREPARED FOR

ADVANCED RESEARCH PROJECTS AGENCY
1400 WILSON BOULEVARD
ARLINGTON, VIRGINIA 22209

THE VIEW, OPINIONS, AND/OR FINDINGS CONTAINED IN THIS REPORT ARE THOSE OF THE AUTHORS AND SHOULD NOT BE CONSTRUED AS AN OFFICIAL DEPARTMENT OF THE ARMY POSITION, POLICY OR DECISION, UNLESS SO DESIGNATED BY OTHER DOCUMENTATION.

UNCLASSIFIED

SECURITY CLASSIFICATION OF THIS PAGE (When Data Entered)

REPORT DOCUMENTATION PAGE

READ INSTRUCTIONS BEFORE COMPLETING FORM

1. REPORT NUMBER — 2. GOVT ACCESSION NO. AD-A100 151	3. RECIPIENT'S CATALOG NUMBER
4. TITLE (and Subtitle) THE QUALIFICATION OF TARGET MATERIALS USING THE INTEGRAL THEORY OF IMPACT	5. TYPE OF REPORT & PERIOD COVERED Interim Report 15 Mar 76 - 15 Dec. 76
	6. PERFORMING ORG. REPORT NUMBER A.R.A.P. Report No. 295
7. AUTHOR(s) C. duP. Donaldson, Ross Contiliano, Claude Swanson	8. CONTRACT OR GRANT NUMBER(s) DAAD05-76-C-0757
9. PERFORMING ORGANIZATION NAME AND ADDRESS Aeronautical Research Associates of Princeton, Inc., 50 Washington Road, Princeton, New Jersey 08540	10. PROGRAM ELEMENT, PROJECT, TASK AREA & WORK UNIT NUMBERS
11. CONTROLLING OFFICE NAME AND ADDRESS Advanced Research Projects Agency 1400 Wilson Boulevard Arlington, Virginia 22209	12. REPORT DATE December 1976
	13. NUMBER OF PAGES 69
14. MONITORING AGENCY NAME & ADDRESS(if different from Controlling Office)	15. SECURITY CLASS. (of this report) UNCLASSIFIED
	15a. DECLASSIFICATION/DOWNGRADING SCHEDULE

16. DISTRIBUTION STATEMENT (of this Report)

Approved for public release, distribution unlimited.

17. DISTRIBUTION STATEMENT (of the abstract entered in Block 20, if different from Report)

18. SUPPLEMENTARY NOTES

19. KEY WORDS (Continue on reverse side if necessary and identify by block number)

Integral Theory of Impact
Impact
Armor
Penetrator
Material Properties

20. ABSTRACT (Continue on reverse side if necessary and identify by block number)

A series of impact tests was conducted in the A.R.A.P. Impact Facility on a wide range of target materials. The penetration data obtained from these tests were used in conjunction with the simple code of the A.R.A.P. Integral Theory of Impact to evaluate two characteristic properties for each target material. One of these properties, E_{*p}, represents the energy absorbed by the target during plastic deformation; the other, E_{*e}, is the elastic energy absorbed by the target. Knowledge of these two

DD FORM 1 JAN 73 1473 EDITION OF 1 NOV 65 IS OBSOLETE

UNCLASSIFIED

SECURITY CLASSIFICATION OF THIS PAGE (When Data Entered)

20. ABSTRACT (continued)

parameters is essential if one is to rationally design either a more effective armor system or a better penetrator.

Coincident with the test program, a theory has been developed which relates these two properties to fundamental material properties which can be measured in static tests. This theory accounts for both strain-rate effects and material property changes due to shear heating. Because it clearly identifies the properties which most influence material response the theory can be used to identify candidate armor (or penetrator) materials.

TABLE OF CONTENTS

CHAPTER 1

Introduction

The purpose of this report is to document the significant results of the first eight months of our research program under contract No. DAAD05-76-C-0757. The object of this portion of the program was to gain an understanding of the underlying physics of the impact process such that one might be able to predict, using a simple model, target material damage under impact conditions. This knowledge is essential if one is to rationally design either a more effective armor system or a better penetrator. The design of a future penetrator must take into account the optimum armor system which may be encountered.

A useful tool for the design of penetrators (or armors) is the simple integral theory of impact which has been developed at A.R.A.P. during the past several years. This theory contains the essential physics of the impact process, satisfies all of the global conservation equations and is contained in a computer code which is simple and inexpensive to operate. The integral theory avoids the gross empiricism of some models and the high cost and complexity of multi-element codes. Its simplicity introduces a degree of economy that makes it reasonable to conduct parametric studies. Availability of predicted trends, rather than single point predictions, greatly facilitates the interpretation of observations and the selection of effective designs. The integral theory can, therefore, be used to guide experimental programs and to select those designs which warrant the details of the large codes.

During the course of our earlier studies, it was determined that for the purpose of calculating target response during impact, it was necessary to determine experimentally at least two characteristic quantities for any target material. One of these quantities, denoted by E_* (the characteristic energy) represented the amount of energy required to put the target material in a hydrodynamic mode. The other quantity, denoted by V_* (a characteristic velocity) was a measure of the elastic energy which could be stored in the target.

Our present results show that an alternative pair of parameters can be used to shed more light on the physics of the impact process. In this alternative, E_* contains at least two components, a quantity E_{*p} which represents the energy absorbed during plastic deformation of the target and a quantity E_{*e} which is the elastic energy absorbed by the target during impact. E_{*p} corresponds to the E_* of our earlier studies and is shown to be roughly constant for a given target material. E_{*e} corresponds to V_* and is shown to be a function of depth of penetration.

The work performed to date and reported upon here consists of two parts:

(1) experimental evaluation of E_{*p} and E_{*e} (or alternatively E_* and V_*) for a broad spectrum of target materials, and

(2) theoretical prediction of the value of each parameter using fundamental material properties.

A series of impact tests was conducted in the A.R.A.P. Impact Facility on sixteen target materials. The penetration data obtained from these tests were used in conjunction with the simple code of the integral theory to evaluate the characteristic properties for each target material. Simultaneously, a theory has been developed which relates the characteristic properties to fundamental material properties, such as hardness and elastic modulus, which can be measured in static tests. This theory accounts for both strain-rate effects and material property changes due to shear heating in the deformation region. Because it clearly identifies the fundamental properties which most influence material response, the theory can be used to identify candidate armor (or penetrator) materials.

In what follows, we will briefly review the integral theory of impact in Chapter 2. The experimental data which have been analyzed to date and the data-theory correlations will be shown in Chapter 3. The development of the theory for E_{*p} and E_{*e} will be given in Chapter 4. Finally, a summary of conclusions will be given in Chapter 5.

CHAPTER 2

Integral Theory for a Rigid Sphere

In this chapter we will outline the equations which are used to evaluate E_* and V_* for a typical target material. The integral theory of impact starts with three basic equations which govern the partition of energy between the center of mass kinetic energy of an impacting projectile and the work done on the target and on the projectile during impact. These equations take a very simple form for the normal impact of an incompressible cubic pellet that remains a rectangular parallelipiped during impact. The equations defining the motion and deformation of such an idealized projectile have been described in earlier reports (Refs. 1 and 2) and will not be repeated here. Instead, we will concentrate on the penetration of a nondeforming sphere - the geometry which was studied in the test program.

Figure 1 schematically depicts the penetration of a semi-infinite target by a nondeforming sphere. The momentum equation for the sphere may be written

$$\frac{d}{dt}(m_p V_c) = - F \tag{1}$$

where F is the total drag force imposed by the target on the projectile, m_p is the projectile mass, and V_c is the center of mass velocity. In this report, we will consider only normal impacts. Hence, the velocity vector, V_c, will always be normal to the surface. Because the projectile is nondeforming and is not spinning, the axial velocity is V_c at every point of the projectile.

If both sides of (1) are multiplied by V_c, the result is an equation for the particle kinetic energy,

$$\frac{d}{dt}\left(m_p \frac{V_c^2}{2}\right) = - FV_c \tag{2}$$

The rate at which work is done on the target is given by:

$$\frac{d}{dt} W_t = FV_c \tag{3}$$

The addition of (2) and (3) shows that for a nondeforming projectile, the initial kinetic energy can only be converted into work done on the target.

The energy transferred to the target is distributed between kinetic energy and other nonkinetic forms of energy depending on the state of the target material. This can be written:

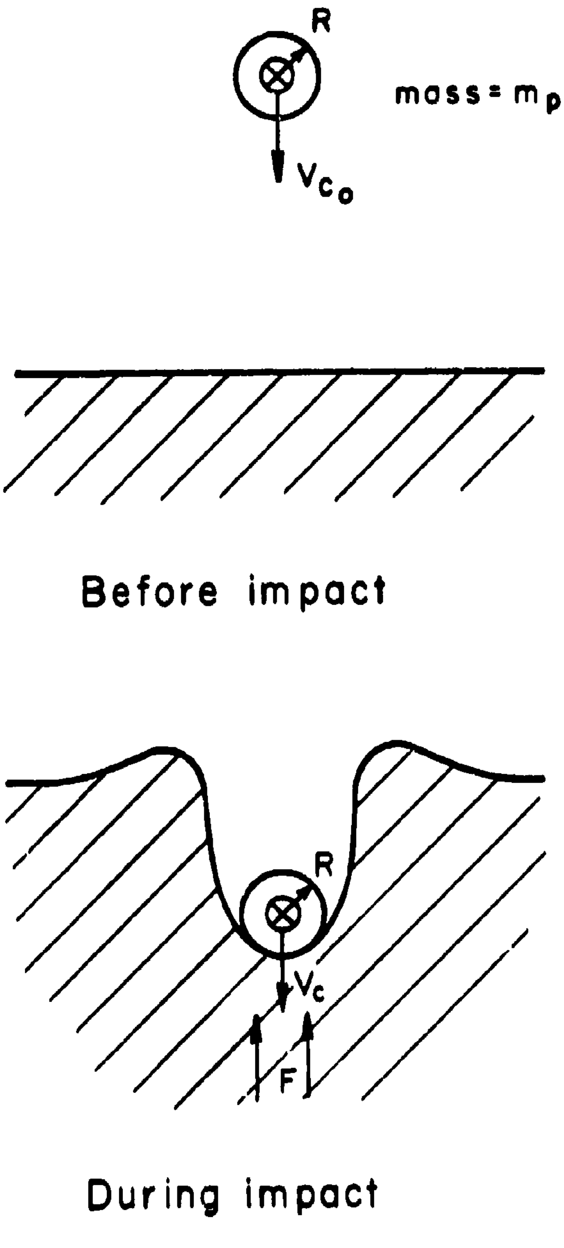

Figure 1

$$\frac{d}{dt} W_t = \frac{d}{dt} KE_t + \frac{d}{dt} U_t \qquad (4)$$

For the rigid sphere, (4) may be written:

$$\frac{d}{dt} W_t = \iint_A \rho_t V_c \left[\frac{C_D \, V_\perp^2(\phi)}{2} + E_*\right] A(\phi) \cos \phi \, dA \qquad (5)$$

where ρ_t is the target mass density, $V_\perp$ is the local velocity normal to the surface of the sphere and is a function of the angle ϕ from the nose, and A is the submerged or interface area which is also a function of ϕ. The integration is taken over the entire submerged area of the sphere. This equation may be taken as a definition for both C_D and E_* and we may roughly identify C_D with the hydrodynamic drag of the target and E_* with the energy required to put the target material into a hydrodynamic mode.

If we equate (3) and (5), we obtain an expression for the total force at the interface:

$$F = \rho_t \iint_A \left[\frac{C_D \, V_\perp^2(\phi)}{2} + E_*\right] A(\phi) \cos \phi \, dA \qquad (6)$$

We see that the force consists of two components. The first component is caused by the acceleration of target material around the sphere. This term dominates when $V_\perp^2 >> E_*$; i.e., target inertia slows the projectile when the velocity is large. The second component is independent of location on the sphere and is due to energy storage in the target material. This term dominates when $E_* >> V_\perp^2$.

If we substitute (6) back into (1), we get the equation of motion for the sphere:

$$m_p \frac{d}{dt} V_c = - \rho_t \iint_A \left(\frac{C_D}{2} \; V_\perp^2(\phi) + E_*\right) A(\phi) \cos \phi \, dA \qquad (7)$$

In addition, if we make the following substitutions:

$$m_p = \frac{4}{3} \pi R^3 \rho_p \qquad (8)$$

$$A(\phi) dA = 2\pi R^2 \sin \phi \, d\phi \qquad (9)$$

and

$$V_\perp = V_c \cos \phi \qquad (10)$$

we get the differential equation:

$$\frac{d}{dt} V_c = -\frac{3}{2} \frac{\rho_t}{\rho_p} \frac{1}{R} \int_0^{\phi_s} \left[\frac{C_D V_c^2}{2} \cos^2\phi + E_*\right] \sin\phi \cos\phi \, d\phi \quad (11)$$

where ϕ_s, the submergence angle, is related to the penetration depth, p, by the equation:

$$\cos\phi_s = 1 - p/R \quad (12)$$

If we perform the area integration in (11), we obtain:

$$\frac{d}{dt} V_c = -\frac{3}{2} \frac{\rho_t}{\rho_p} \frac{1}{R} \left\{ \frac{C_D V_c^2}{2} \left(\frac{1 - \cos^4\phi_s}{4} \right) + E_* \frac{\sin^2\phi_s}{2} \right\} \quad (13)$$

Substitution of (12) into (13) yields a relation between V_c and p. A second equation between these two parameters is given by the definition of velocity:

$$\frac{dp}{dt} = V_c \quad (14)$$

Equations (12) through (14) can be integrated simultaneously to yield $p(t)$ and $V_c(t)$. The integration proceeds from $t = 0$ to $t = t_*$, the time at which V_c is reduced to V_*.†

Three parameters appear in these integral relations; C_D, E_* and V_*. If one is known, then the equations can be used to evaluate the other two for a given impact velocity and crater depth. The hydrodynamic drag coefficient for a sphere is of order unity and varies within relatively narrow bounds. In our previous studies of deforming particles in supersonic flowfields (e.g., water drops in shock layers) we have obtained good correlation between theory and data using $C_D = 2$. This value can be obtained using the Newtonian approximation for the pressure induced on the surface of a grossly deformed projectile - the limiting shape being a flat disk. Newtonian theory, to first approximation, states that the force induced on the surface is due to the destruction of the normal component of momentum. For a flat disk, the normal momentum is $\rho_t V_c^2$ and, therefore,

$$F_{DRAG} = \rho_t V_c^2 A_{disk} \quad (15)$$

If we substitute (15) into the equation which usually defines the drag coefficient $C_D = F_{DRAG}/\rho_t V_c^2 A/2$ we see that $C_{D_{disk}} = 2$.

If we apply the Newtonian approximation to a rigid sphere, we find that the drag force is given by:

†An alternative approach in which the integration proceeds to $V_c = 0$ and an elastic energy term is included in (13) is discussed in Chapter 4.

$$F_{DRAG} = 2\pi \int_0^{\pi/2} \rho_t V_\perp^2 \cos\phi \, R^2 \sin\phi \, d\phi$$

or

$$F_{DRAG} = 2\pi R^2 \int_0^{\pi/2} \rho_t V_c^2 \cos^3\phi \sin\phi \, d\phi$$

Finally,

$$F_{DRAG} = \frac{\pi R^2}{2} \rho_t V_c^2$$

and

$$C_{D_{sphere}} = 1$$

The Newtonian approximation is valid only at the outer edge of the disturbed region and not at the projectile surface, although this distinction is generally ignored. To obtain the pressure at the surface, a centrifugal force term must be included in the momentum equation to account for curvature effects. This term has the net effect of reducing C_D to approximately 0.75 for a sphere.

The analysis which is discussed in the next chapter was based on $C_D = 2$. In the future, the analysis will be repeated using the more appropriate value of C_D for the sphere.

In either case, with C_D = constant, we can return to (13) and (14) and numerically solve these equations to obtain the combination of V_* and E_* which best matches the data for each target material.

CHAPTER 3

Experimental Results

This chapter describes the A.R.A.P. Impact Facility, summarizes the test program, presents the experimental data and the evaluation of E_* and V_* for each of the target materials.

A.R.A.P. Impact Facility

Figure 2 depicts schematically the A.R.A.P. Impact Facility. This facility consists of a mounted weapon, and enclosed test tube and test chamber. The weapon used for most of the tests is a Winchester 270 caliber, smooth bore rifle which is permanently mounted to a support and is bore-sighted on the target. Cartridges are hand-loaded using Hercules 2400 gunpowder and the rifle is remotely fired.

The projectiles are 0.250-inch diameter balls. All testing to date, using 0.250-inch diameter balls, has been done with tungsten carbide balls. Future tests will include several other ball materials including lead, aluminum, and glass. The balls are mounted at the end of the cartridge using a bore-fitting Lexan sabot. For tungsten carbide balls, the velocity range of the rifle is 700 to 5,000 feet per second.

The sabot is manufactured in sections. It separates aerodynamically upon leaving the nozzle and each piece hits the stripper plate located at the downstream end of the test tube. Only the projectile enters the test chamber and hits the target.

The target is mounted in a permanent holder attached to the downstream end of the test chamber. Most of the targets have been circular disks with a nominal diameter of 6 inches and a thickness of 1 inch. However, the holder is versatile and can accommodate any shape which can fit within a 6-inch diameter circle.

The velocity of the ball is measured using a Schmidt-Weston Chronograph. Two light screens, two feet apart, sense the passage of the ball using a photo resistor element. The flight path of the ball is illuminated by light which passes through slits in a shelf in the test chamber. The shadow produced by the ball on the first screen triggers a counter and a shadow on the second screen stops the counter. A digital readout of the velocity is provided on the display board.

In order to extend the low velocity range of the facility, we also use a Power Line 880 Air Gun. This rifle has a velocity range between 160 and 740 feet per second when firing 0.156 and 0.172 inch diameter tungsten carbide and chrome steel balls. The lower limit of velocity is set by the chronograph.

A.R.A.P. IMPACT FACILITY

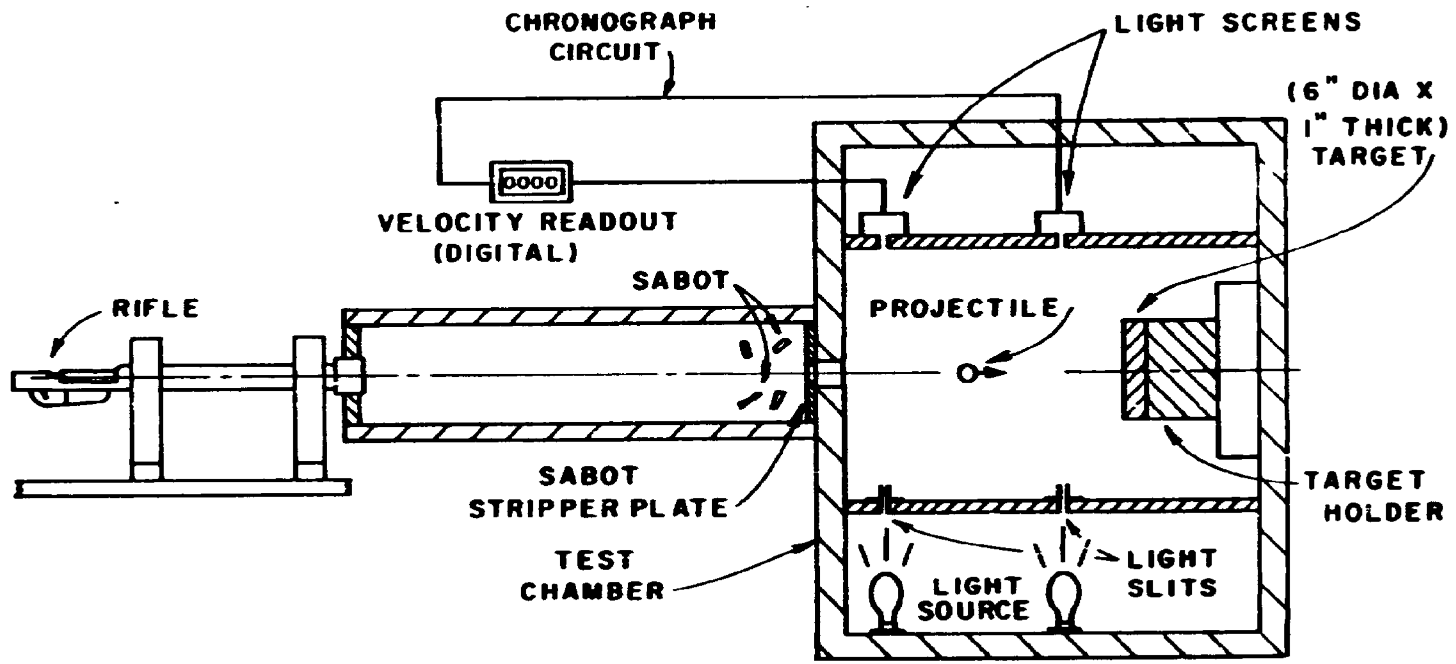

Gun	Projectile	Velocity range
Winchester 270 Smooth bore rifle	.25" WC ball with Lexan sabot	700-5000 fps
Power Line 880 Air gun	5/32" & 11/64" WC or chrome steel ball	160-740 fps

Figure 2

For each target material, tests were also conducted by dropping a ball from the laboratory ceiling onto the target. From a height of approximately 14 feet, the impact velocity was computed to be 28 feet per second.

Test Program

Table 1 summarizes the status of the test program. A total of 141 tests have been conducted on 16 target materials. These targets include 7 nearly pure metals: aluminum, cadmium, copper, lead, iron, silicon, and zinc; 3 alloys; mild steel, hard armor steel and armor aluminum; and a range of ceramics and composites, including glass, acrylic, polycarbonate, sodium chloride, boron carbide and Kevlar.

Table 1 shows the number of tests and the velocity range for each target material. The lower limit of the velocity range is near the chronograph limit. The upper limit is set by a criterion which limits the crater depth to half the target thickness in order to minimize backface effects.

The status of the test program is shown by the three columns on Table 1. The first column shows that all of the test targets have been fabricated except for silicon and boron carbide. These targets will be completed shortly. Testing has been completed for each of the target materials except the above-mentioned two and Kevlar.

The target material properties E_* and V_* have been evaluated for the nine materials which are checked in the analysis column of Table 1. These results are described below. The remaining materials will be completed in the near future.

Data Analysis

Figure 3 shows the penetration data for a soft aluminum (1100-F) target. The figure presents maximum crater depth normalized by projectile diameter versus projectile impact velocity. Data are shown for both tungsten carbide and steel balls. The impact velocity varied from 28 feet per second to 1700 feet per second. For the latter velocity, the ball remained embedded in the target and the maximum crater depth was slightly in excess of half the target thickness. In all of the tests, there was no measurable plastic deformation of the ball after impact.

The solid lines show the computed penetration using the equations discussed in Chapter 2 and the model parameters $E_* = 79$ BTU/lbm and $V_* \cong 0$ ft/sec. The correlation between theory and data is very good for a two-decade range of impact velocity and a factor of two range in density ratio. All of these computations are based on $C_D = 2$. The effect of using a more appropriate drag coefficient for a rigid sphere $(C_D = 1)$ will be described at the end of this chapter.

PROGRAM SUMMARY

TARGET MATERIAL	STATUS			NO. TEST TO DATE	IMPACT VELOCITY
	TARG.	TEST	ANAL.		
ALUMINUM (1100-F)	✓	✓	✓	10	160-1701
CADMIUM	✓	✓	✓	10	159-1491
COPPER (ETP)	✓	✓	✓	10	161-2483
IRON (Class 40 gray)	✓	✓	✓	11	167-2892
LEAD	✓	✓	✓	14	161-1174
STEEL (1020-H.R.)	✓	✓	✓	10	163-4336
ZINC	✓	✓	✓	10	164-2680
POLYCARBONATE (G.E. Lexan)	✓	✓	✓	10	162-1811
GLASS (Corning-Pyrex)	✓	✓		9	198-1087
ACRYLIC (Am. Cyan. acrylite)	✓	✓		10	162-1397
SALT (NaCl)	✓	✓	✓	14	161-1282
SILICON				4	916-1381
ARMOR STEEL (RHA)	✓	✓		7	193-2082
ARMOR ALUMINUM (5083)	✓	✓		7	196-2326
KEVLAR	✓			1	1235
BORON CARBIDE				4	~1000-1900
				141	

Table 1

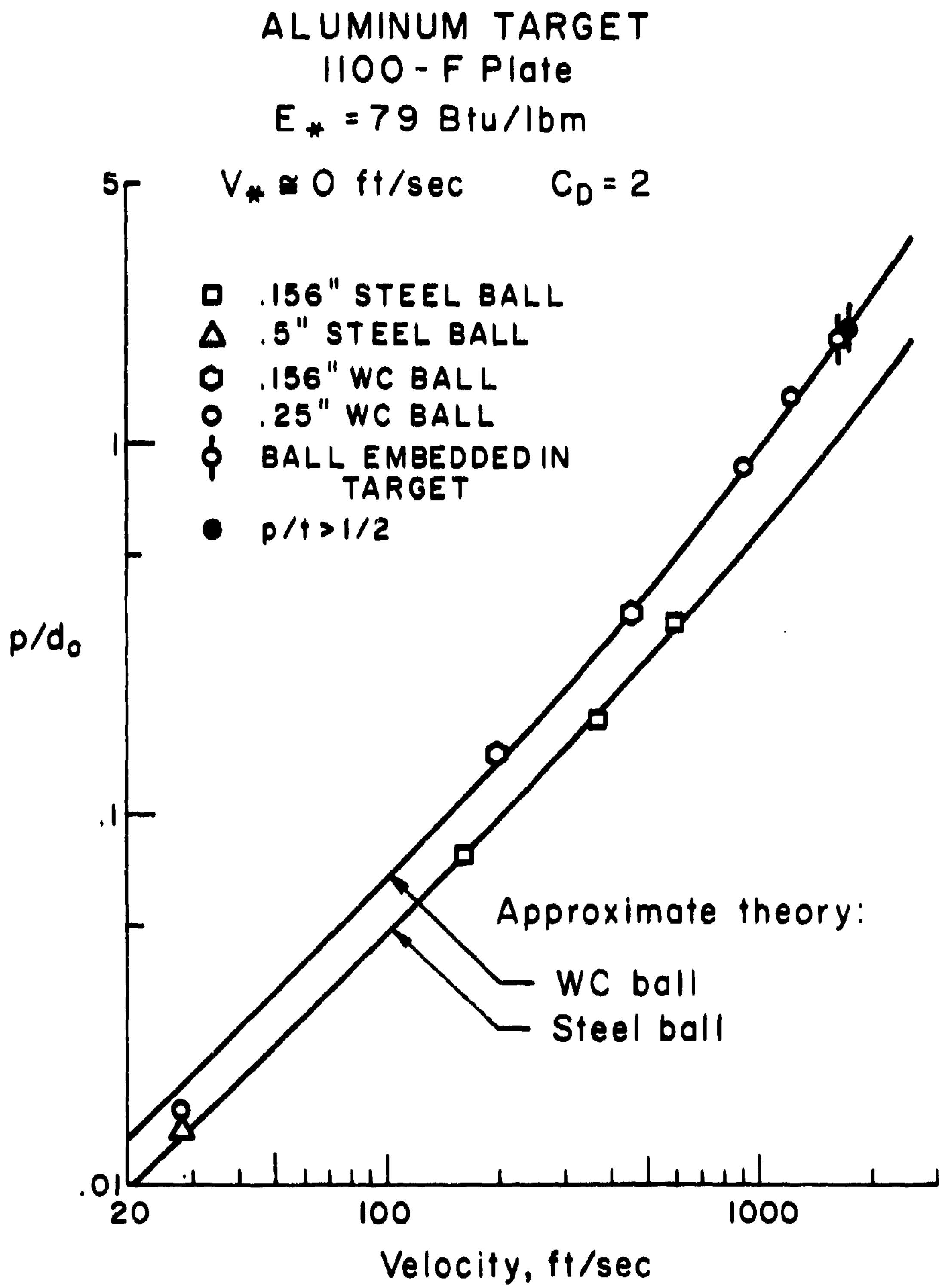
ALUMINUM TARGET
1100 - F Plate
E* = 79 Btu/lbm
V* ≅ 0 ft/sec
CD = 2
.156" STEEL BALL
.5" STEEL BALL
.156" WC BALL
.25" WC BALL
BALL EMBEDDED IN TARGET
p/t > 1/2
p/do
5
1
.1
.01
20
100
1000
Velocity, ft/sec
Approximate theory:
WC ball
Steel ball

Figure 3

Figure 4 shows the experimental value of E_* for each test condition as a function of the normalized penetration. This value of E_* is obtained numerically by matching the measured penetration with theoretical computations for each impact test. It can be seen that the data fall within a narrow band and that E_* is approximately constant. The one exception to this result is a shallow penetration data point which is relatively inaccurate. The solid line shows the average value of $E_* = 79$ BTU/lbm and it is this value which was used in the theoretical computations in figure 3.

The dashed curve shows the present theoretical prediction for E_* . This theory is described in the next chapter. For the present, note that the upward slope of the curve for decreasing p/do is the elastic contribution to E_* . The asymptotic value for large p/do is the plastic contribution to E_* .

Figure 5 shows the penetration data for pure, open cast cadmium. The correlation between theory and data is good for velocities below 1,000 feet per second using $E_* = 27$ BTU/lbm and $V_* \cong 0$ ft/sec. For larger velocities, the theory underpredicts the crater depth. For these velocities, the dominant contribution to the drag force is inertia of the target material. Because we used $C_D = 2$ rather than $C_D = \sim 1$ for these computations, we have overpredicted the drag, and, therefore, underpredicted the penetration. For lower velocities, E_* is the dominant factor and C_D has only a slight effect. Examples of the effect of C_D are given at the end of this chapter.

Figure 6 shows the computed values of E_* . Again, because of the C_D effect, the theory overpredicts the value of E_* for large penetrations. It will be shown later that a lower value of C_D will tend to increase the computed value of E_* for the large p/do . To a first approximation, the average value of E_* for cadmium is 27 BTU/lbm.

Figures 7 and 8 show the data and theoretical computations for hot rolled electrolytic tough pitch copper. The correlation between theory and data is good. To a first approximation $E_* = 35$ BTU/lbm and $V_* \cong 0$ ft/sec.

Figures 9 and 10 show the data and theoretical computations for Class 40 gray cast iron. Good correlation between theory and data is obtained using $E_* = 133$ BTU/lbm and $V_* = 25$ ft/sec.

The results for pure, open cast lead targets are shown in figures 11 and 12. Lead has the lowest value of E_* of all the materials tested. Hence, the drag force on the projectile is primarily due to inertia of the lead target. We have already concluded that $C_D = 2$ is inappropriate for a rigid sphere and, therefore, it is not surprising that the theory underpredicts the penetration for large velocities, the regime where inertial effects are dominant. Note that some of the lead targets were

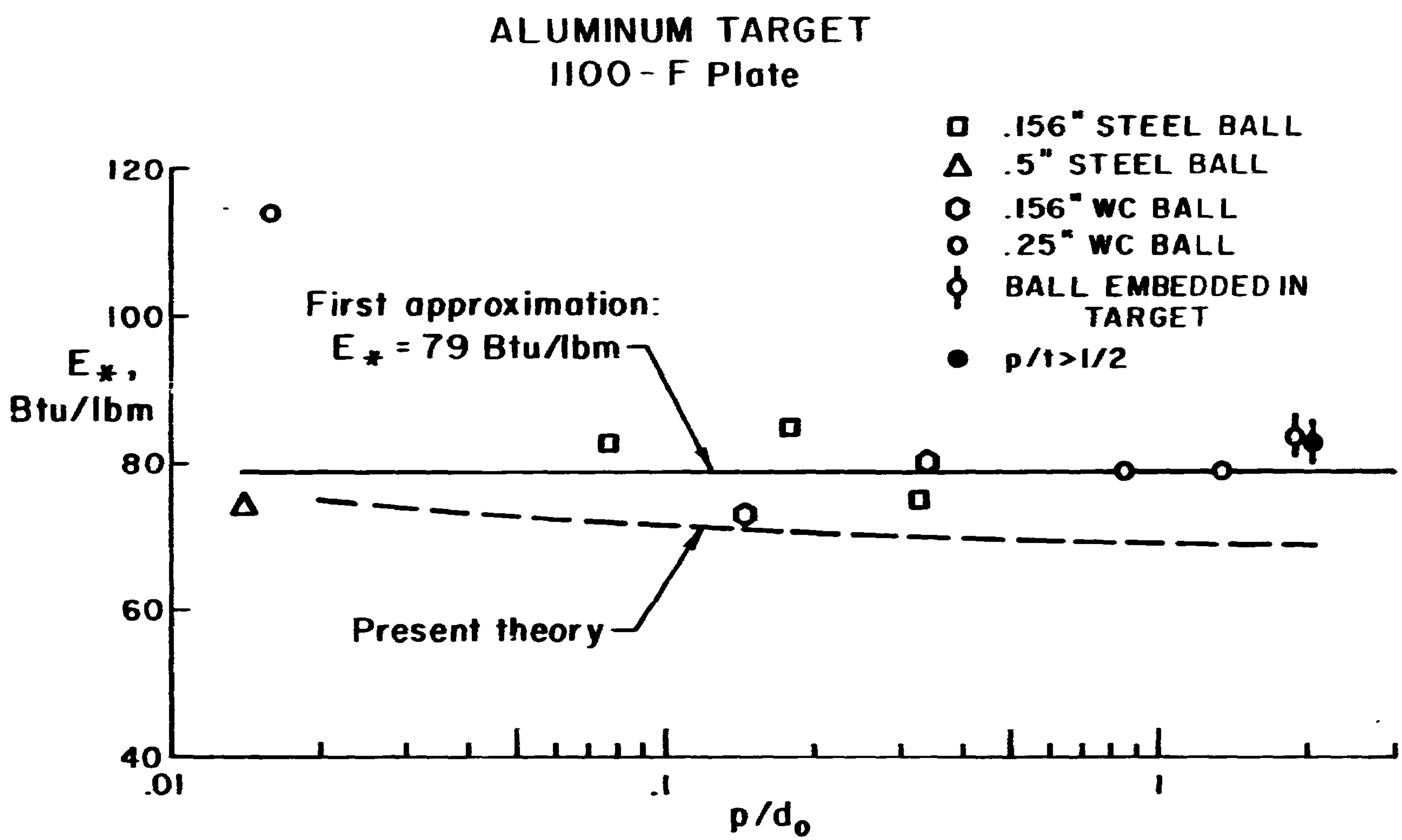
ALUMINUM TARGET
1100 - F Plate
.156" STEEL BALL
.5" STEEL BALL
.156" WC BALL
.25" WC BALL
BALL EMBEDDED IN TARGET
p/t>1/2
First approximation:
$E_* = 79$ Btu/lbm
Present theory
E_*, Btu/lbm
120
100
80
60
40
.01
.1
1
p/d_o

Figure 4

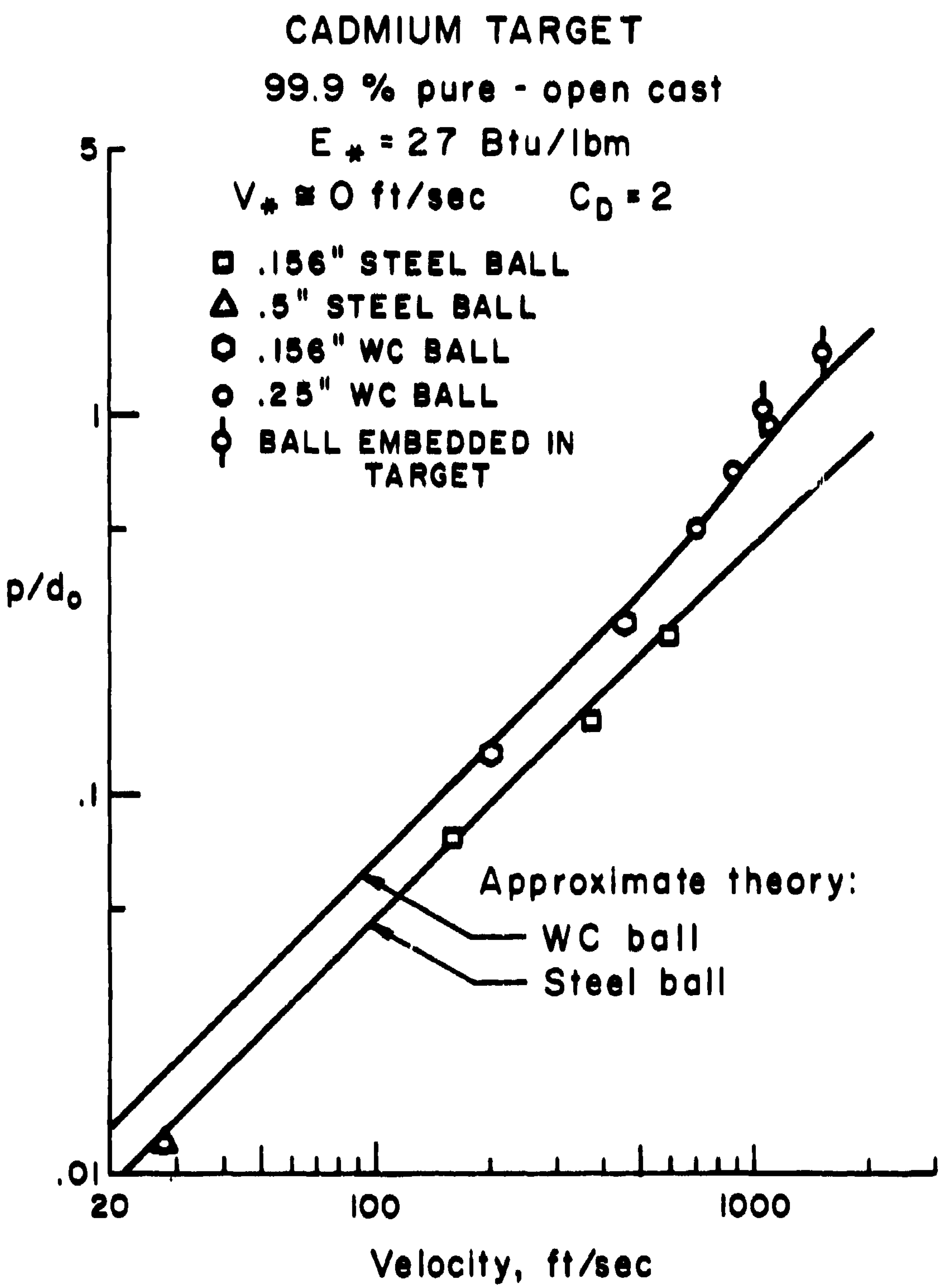
CADMIUM TARGET
99.9 % pure - open cast
E * = 27 Btu/lbm
V* ≅ 0 ft/sec C D = 2
.156" STEEL BALL
.5" STEEL BALL
.156" WC BALL
.25" WC BALL
BALL EMBEDDED IN TARGET
p/d o
Approximate theory:
WC ball
Steel ball
5
1
.1
.01
20
100
1000
Velocity, ft/sec

Figure 5

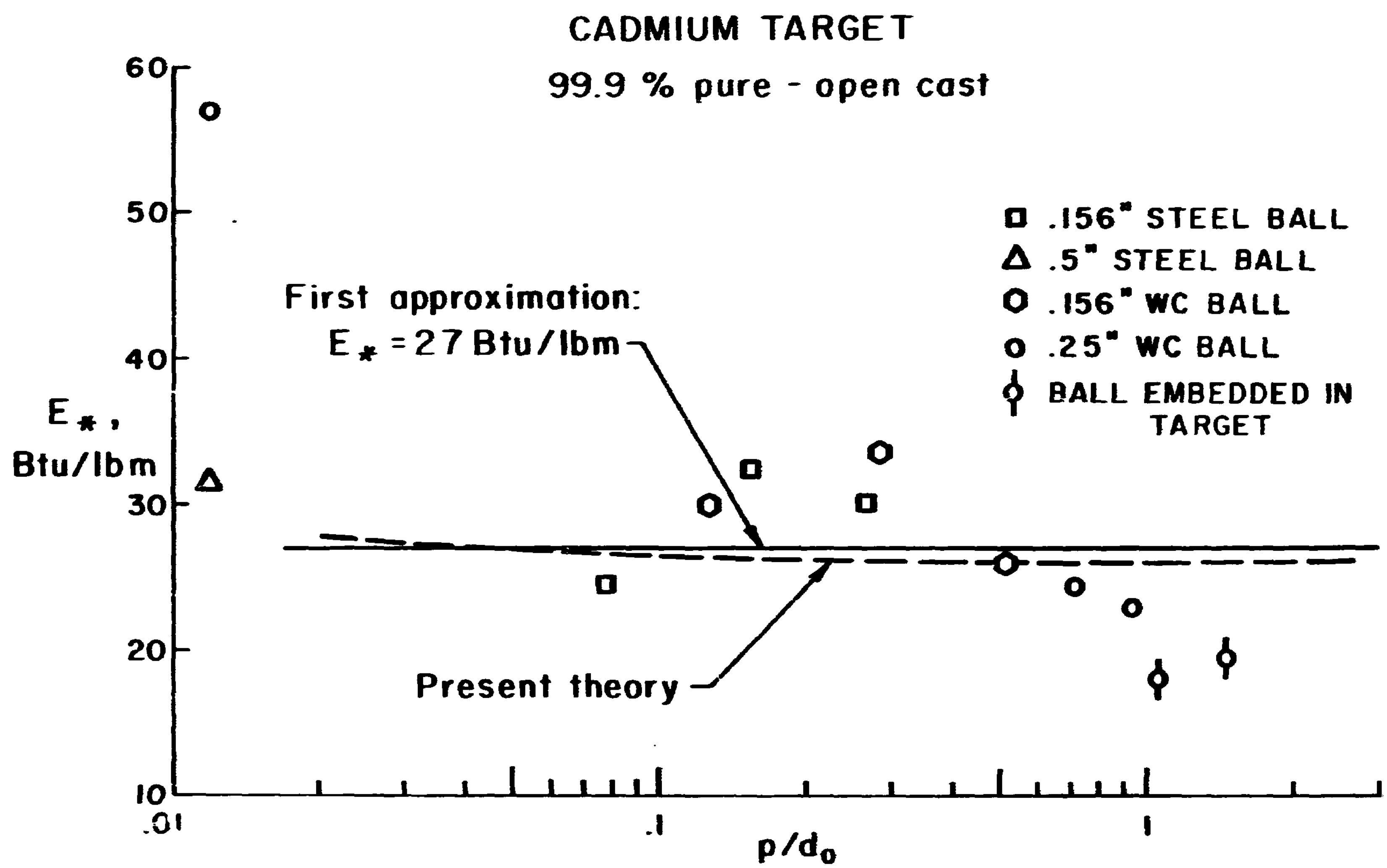
CADMIUM TARGET
99.9 % pure - open cast
60
50
40
30
20
10
E*,
Btu/lbm
First approximation:
E* = 27 Btu/lbm
Present theory
.156" STEEL BALL
.5" STEEL BALL
.156" WC BALL
.25" WC BALL
BALL EMBEDDED IN TARGET
.01
.1
1
p/d0

Figure 6

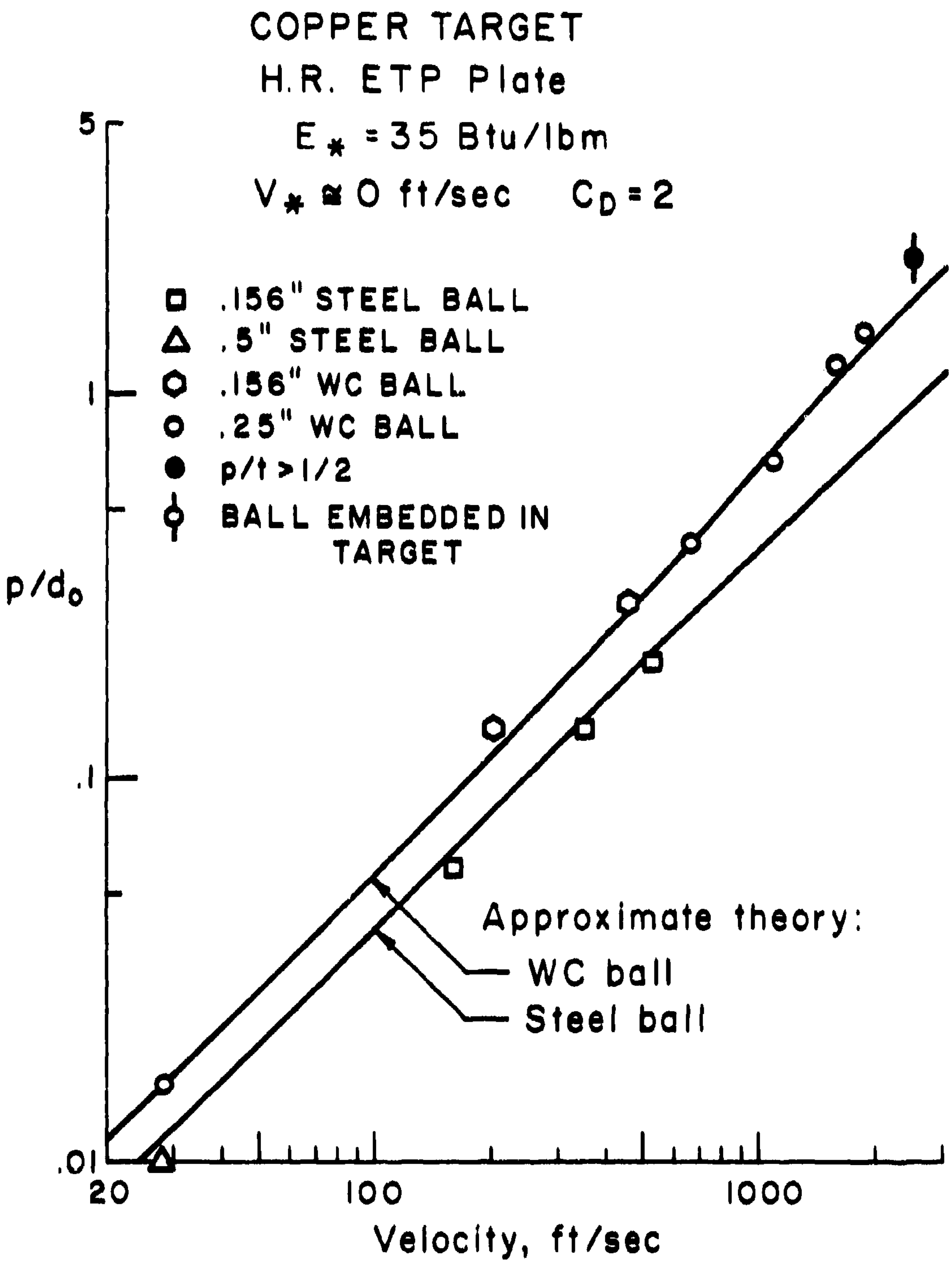
COPPER TARGET
H.R. ETP Plate
E* = 35 Btu/lbm
V* ≅ 0 ft/sec   CD = 2
.156" STEEL BALL
.5" STEEL BALL
.156" WC BALL
.25" WC BALL
p/t > 1/2
BALL EMBEDDED IN TARGET
p/do
5
1
.1
.01
20
100
1000
Velocity, ft/sec
Approximate theory:
WC ball
Steel ball

Figure 7

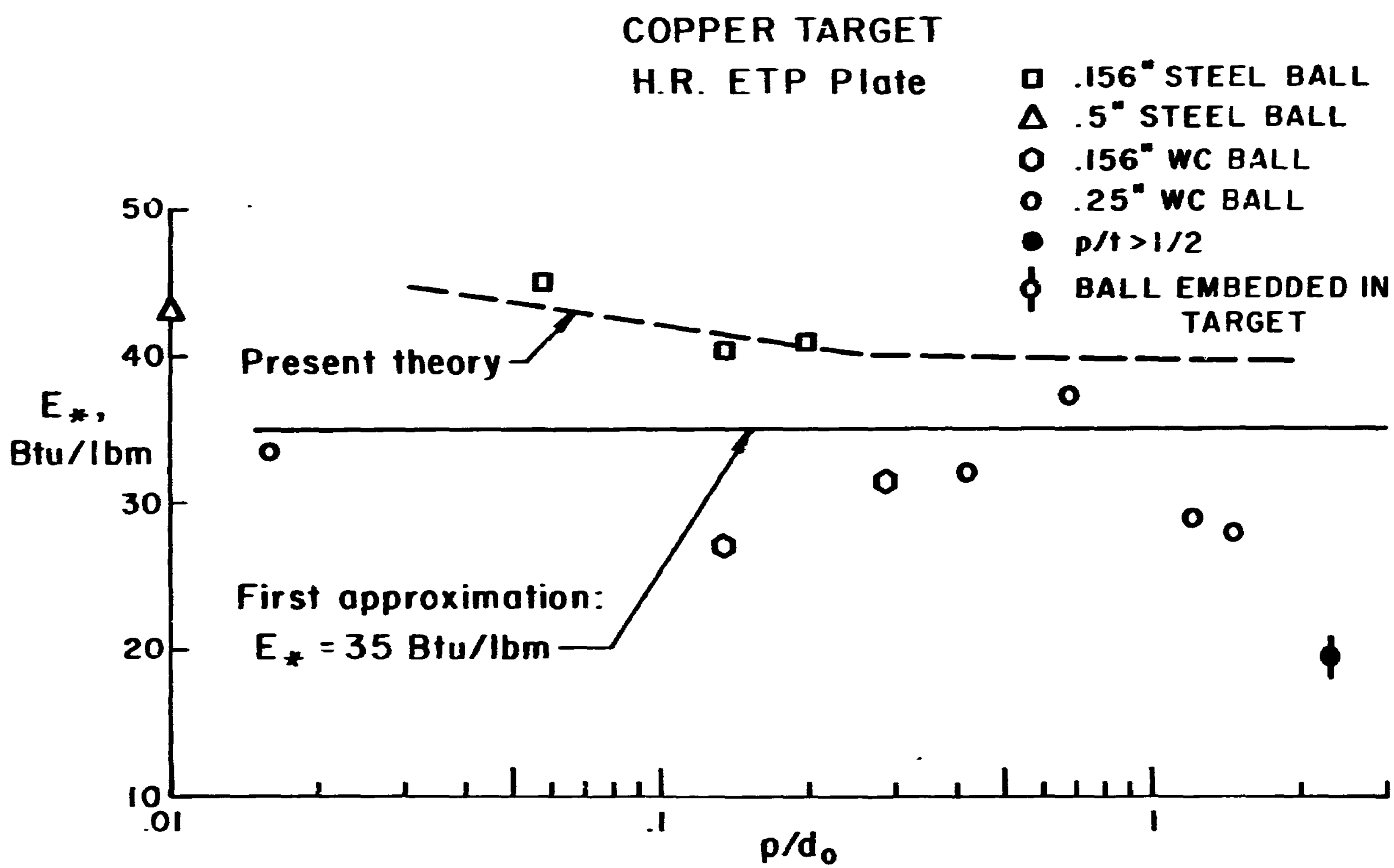
COPPER TARGET
H.R. ETP Plate
.156" STEEL BALL
.5" STEEL BALL
.156" WC BALL
.25" WC BALL
p/t > 1/2
BALL EMBEDDED IN TARGET
Present theory
First approximation:
E* = 35 Btu/lbm
E*, Btu/lbm
50
40
30
20
10
.01
.1
1
p/do

Figure 8

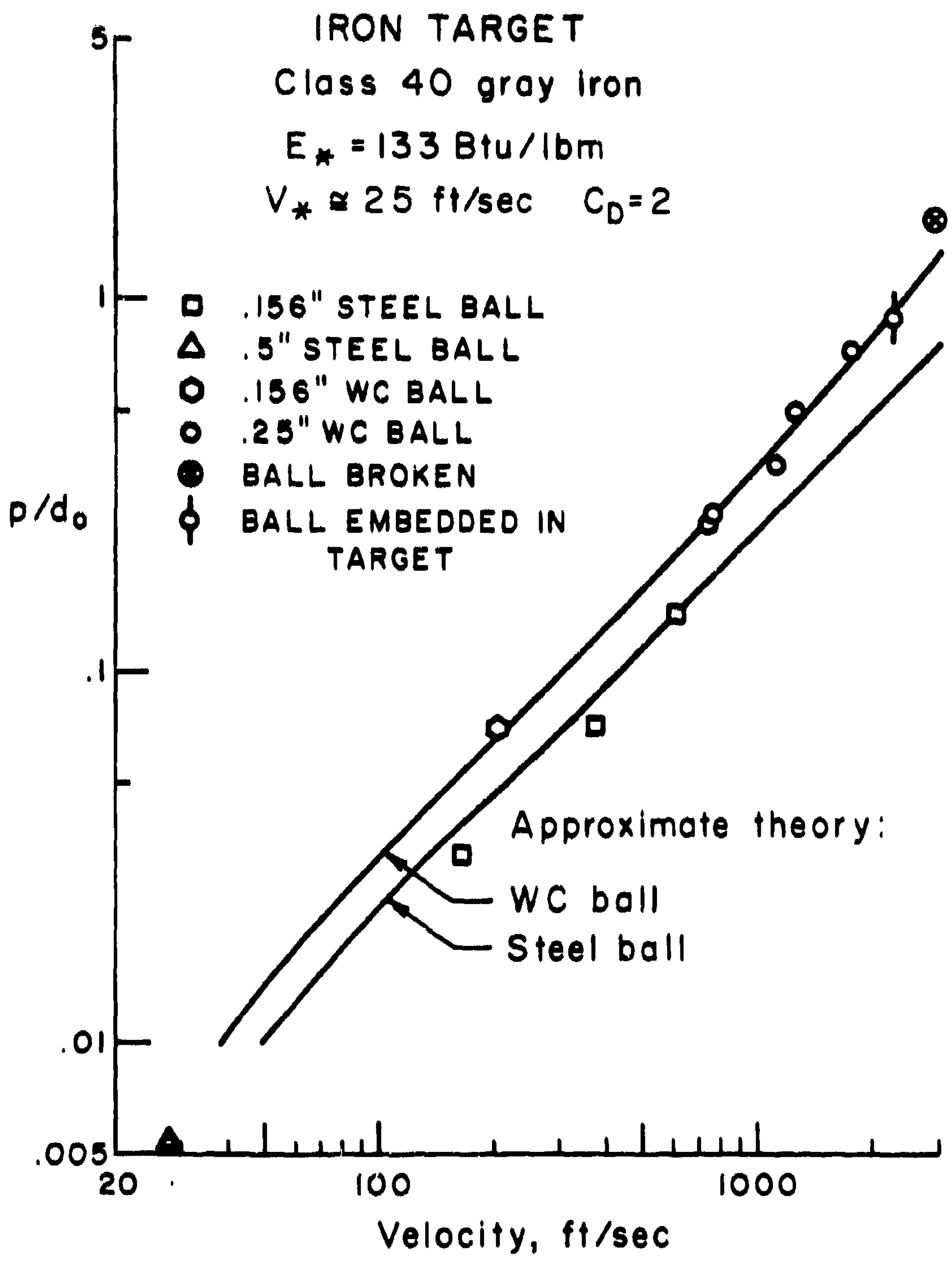

IRON TARGET
Class 40 gray iron
$E_* = 133$ Btu/lbm
$V_* \cong 25$ ft/sec $C_D = 2$
.156" STEEL BALL
.5" STEEL BALL
.156" WC BALL
.25" WC BALL
BALL BROKEN
BALL EMBEDDED IN TARGET
p/d_0
5
1
.1
.01
.005
20
100
1000
Velocity, ft/sec
Approximate theory:
WC ball
Steel ball

Figure 9

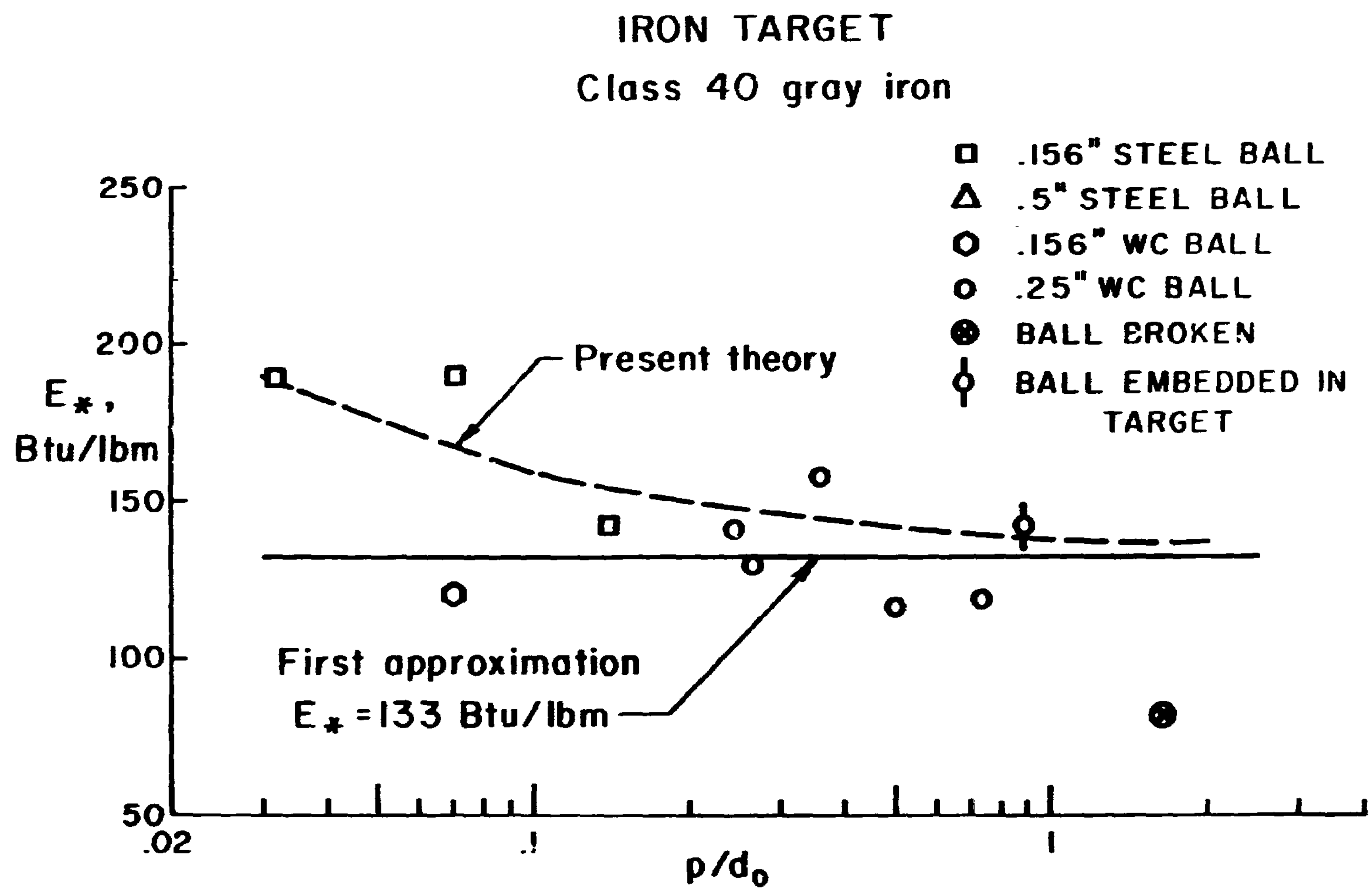
IRON TARGET
Class 40 gray iron
.156" STEEL BALL
.5" STEEL BALL
.156" WC BALL
.25" WC BALL
BALL BROKEN
BALL EMBEDDED IN TARGET
Present theory
First approximation
E* =133 Btu/lbm
E*, Btu/lbm
250
200
150
100
50
.02
.1
1
p/d0

Figure 1[illegible]

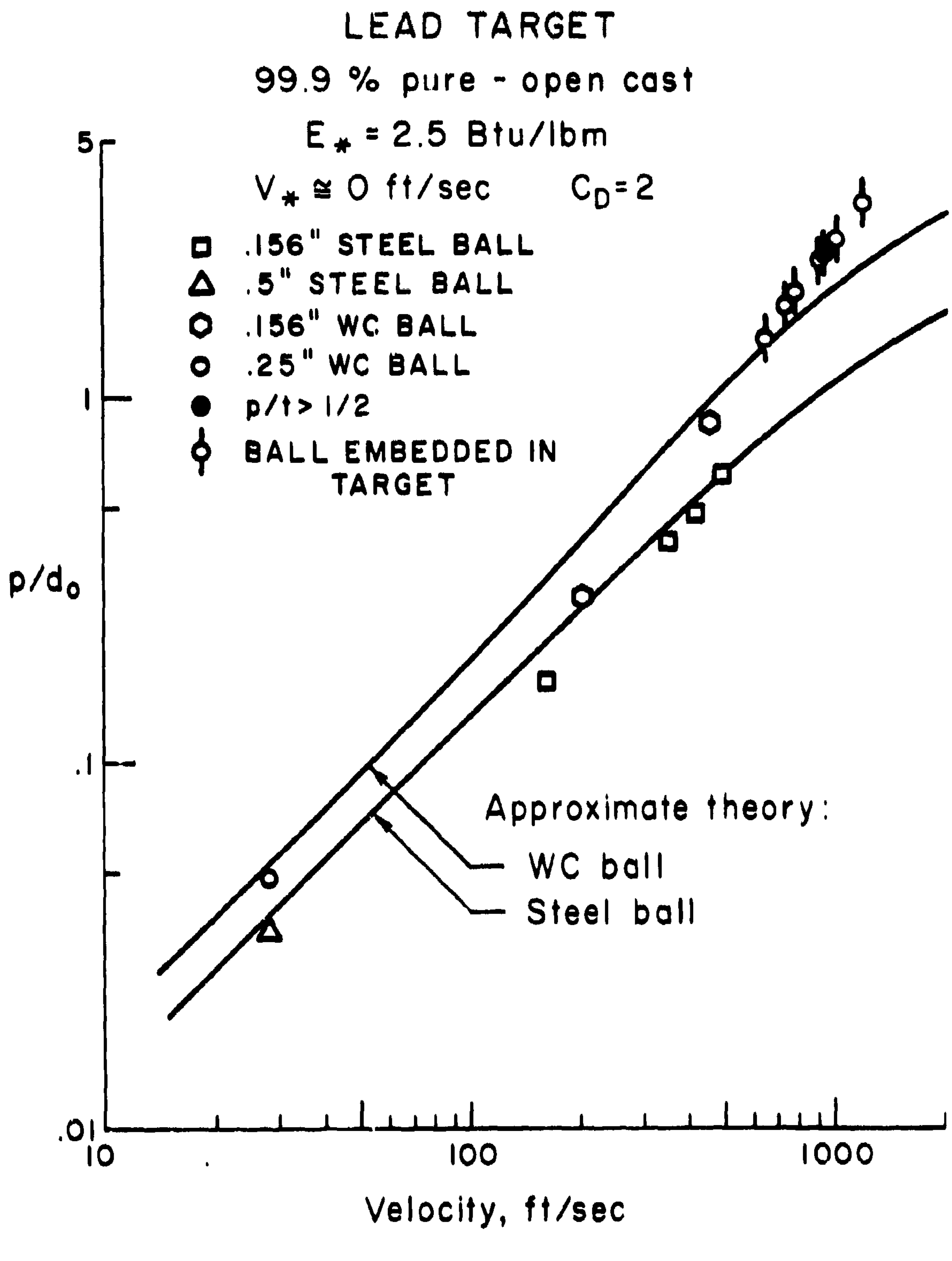
LEAD TARGET
99.9 % pure - open cast
E* = 2.5 Btu/lbm
V* ≅ 0 ft/sec   CD = 2
.156" STEEL BALL
.5" STEEL BALL
.156" WC BALL
.25" WC BALL
p/t > 1/2
BALL EMBEDDED IN TARGET
p/do
Approximate theory:
WC ball
Steel ball
5
1
.1
.01
10
100
1000
Velocity, ft/sec

Figure 11

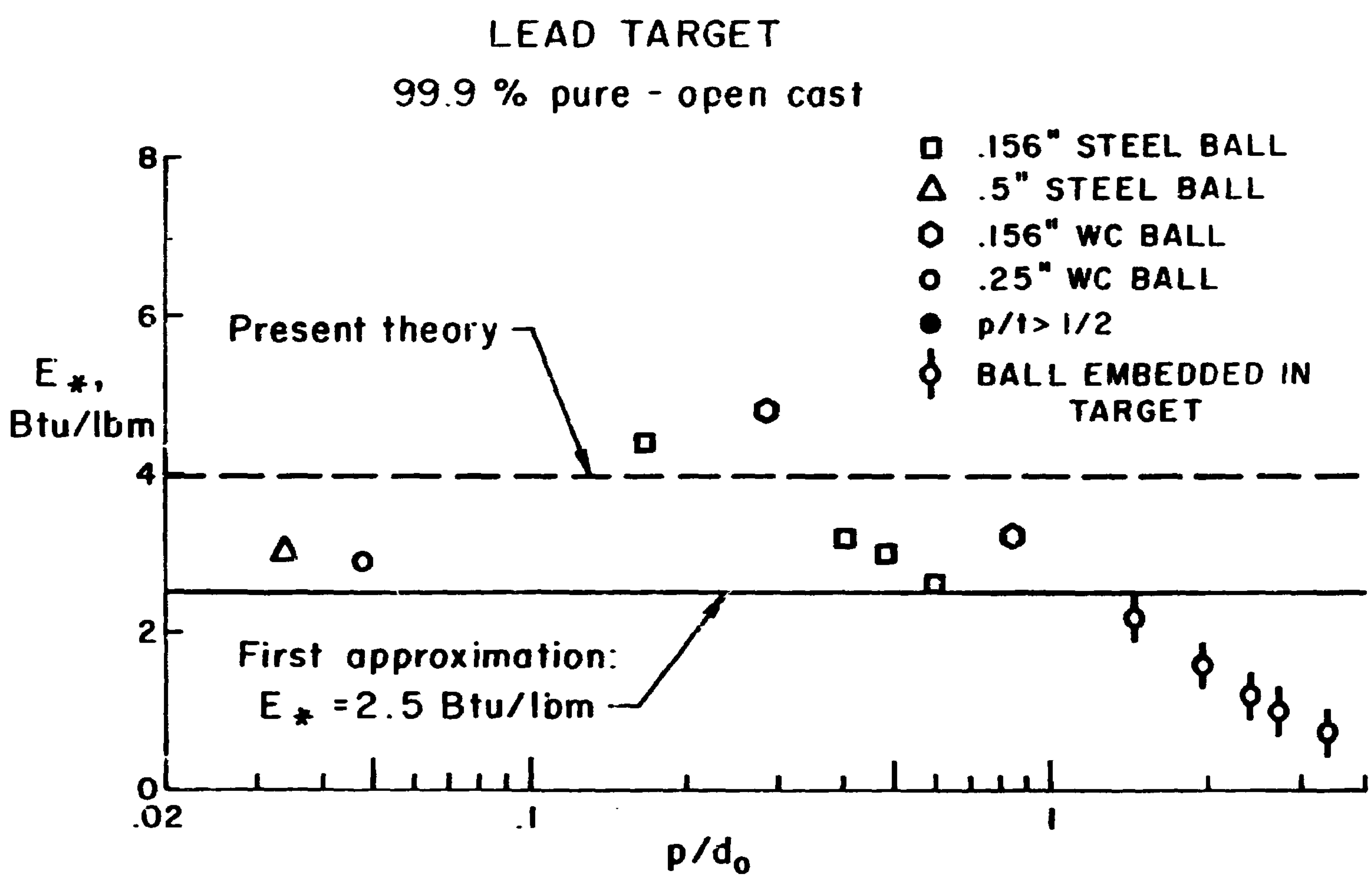
LEAD TARGET
99.9 % pure - open cast
□ .156" STEEL BALL
△ .5" STEEL BALL
⬡ .156" WC BALL
o .25" WC BALL
● p/t> 1/2
BALL EMBEDDED IN TARGET
Present theory
First approximation:
E_* =2.5 Btu/lbm
E_*, Btu/lbm
8
6
4
2
0
.02
.1
1
p/d_o

Figure 12

2.5 inches thick. Hence, open symbols are shown for deeper penetrations than the closed symbol in figure 11.

Figures 13 and 14 show the results for mild steel (H.R. 1020), and figures 15 and 16 are for pure, open-cast zinc. The correlation between theory and data is good for each metal. For steel, $E_* = 165$ BTU/lbm and $V_* = 50$ ft/sec. Note that the rigid particle correlation is also good for the projectiles which fractured upon impact. This is because the tungsten carbide ball has had very little deformation prior to brittle fracture. For zinc, $E_* = 58$ BTU/lbm and $V_* \cong 0$ ft/sec.

The final material for which data analysis is complete is sodium chloride. Salt is the most brittle of the targets discussed in this chapter. Figure 17 shows very good correlation between theory and data for $E_* = 82$ BTU/lbm and $V_* \cong 0$ ft/sec. The computed values for E_* are shown in figure 18. There is more scatter in the data which is to be expected from the brittle nature of the target material. However, most of the data do lie in a band between $E_* = 70$ BTU/lbm and $E_* = 90$ BTU/lbm.

Table 2 summarizes the target material properties. The experimental and theoretical values of E_* are contained in the last two columns. The basis for the theoretical values is described in the next chapter. The experimentally obtained values of E_* are shown for the 8 materials described above, based on $C_D = 2$ and for two materials (polycarbonate and silicon) for which data analysis is not complete. The values in parentheses are the E_* values for copper and lead based on $C_D = 1$.

The agreement between theory and data for E_* is excellent. Note that preliminary results for typical armor materials show that $E_* \cong 200$ BTU/lbm . Also, note that a material has been tested, boron carbide, which exhibits $E_* \cong 1200$ BTU/lbm . The basis for these calculations and their implication is described in the next chapter.

C_D Effects

We have noted that all of the computations described above were based on a constant value of the hydrodynamic drag coefficient appropriate for a deformed projectile ($C_D = 2$) . A more appropriate value for a rigid sphere is $C_D = 1$. We have investigated the effect of C_D for two materials. Figure 19 shows the data-theory correlation for the copper target. The dashed curve is for $C_D = 2$ and is reproduced from figure 7. The solid curve is for $C_D = 1$ and results in much better correlation with the data. To first approximation, the value of E_* increases about 9% when C_D is reduced from 2 to 1.

Figure 20 shows the computed value for E_* for $C_D = 1$. This curve (compared with figure 8) shows that E_* is nearly constant for large p/do .

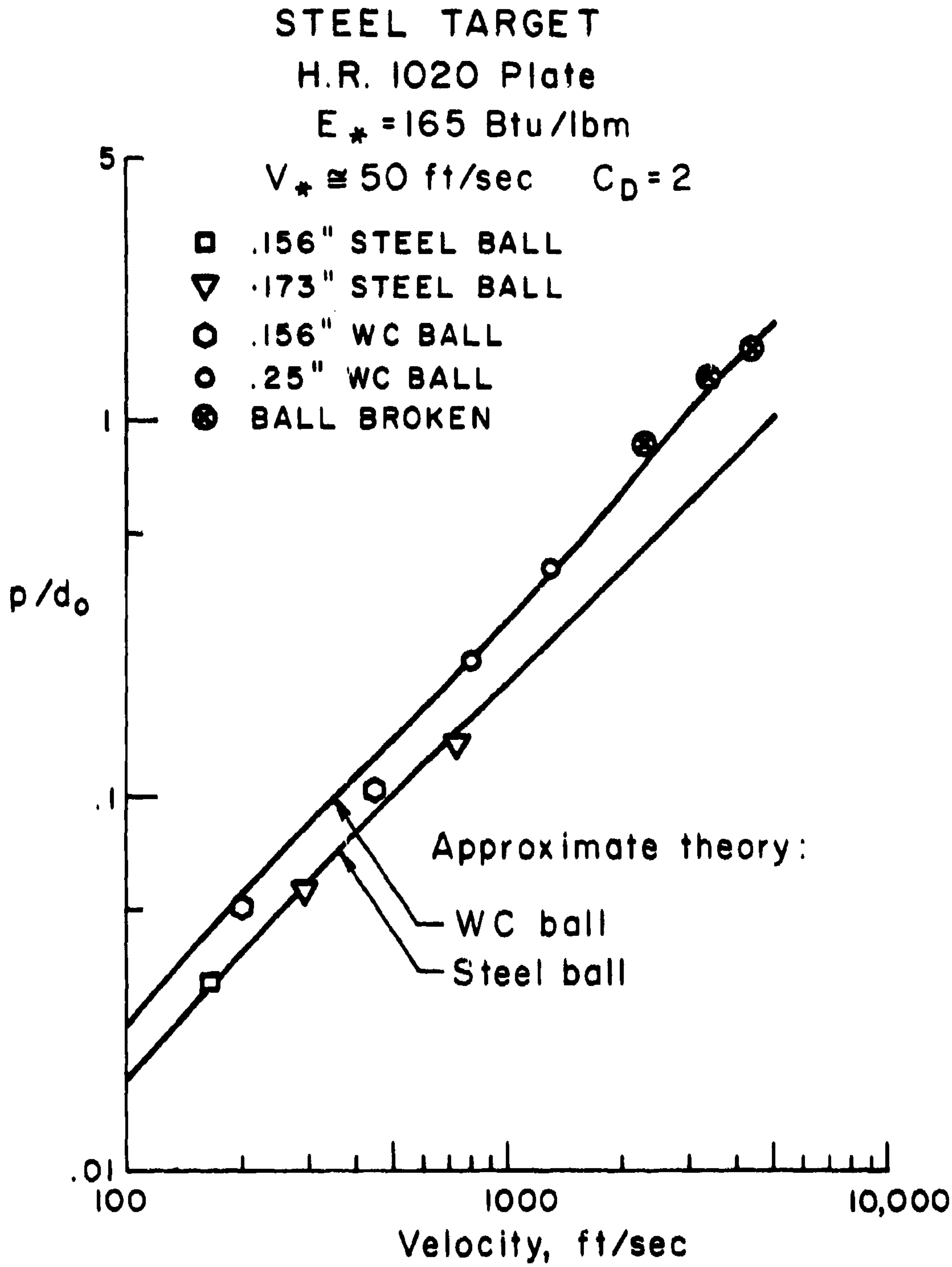

STEEL TARGET
H.R. 1020 Plate
E* = 165 Btu/lbm
V* ≅ 50 ft/sec   CD = 2
.156" STEEL BALL
.173" STEEL BALL
.156" WC BALL
.25" WC BALL
BALL BROKEN
5
1
.1
.01
p/do
Approximate theory:
WC ball
Steel ball
100
1000
10,000
Velocity, ft/sec

Figure 13

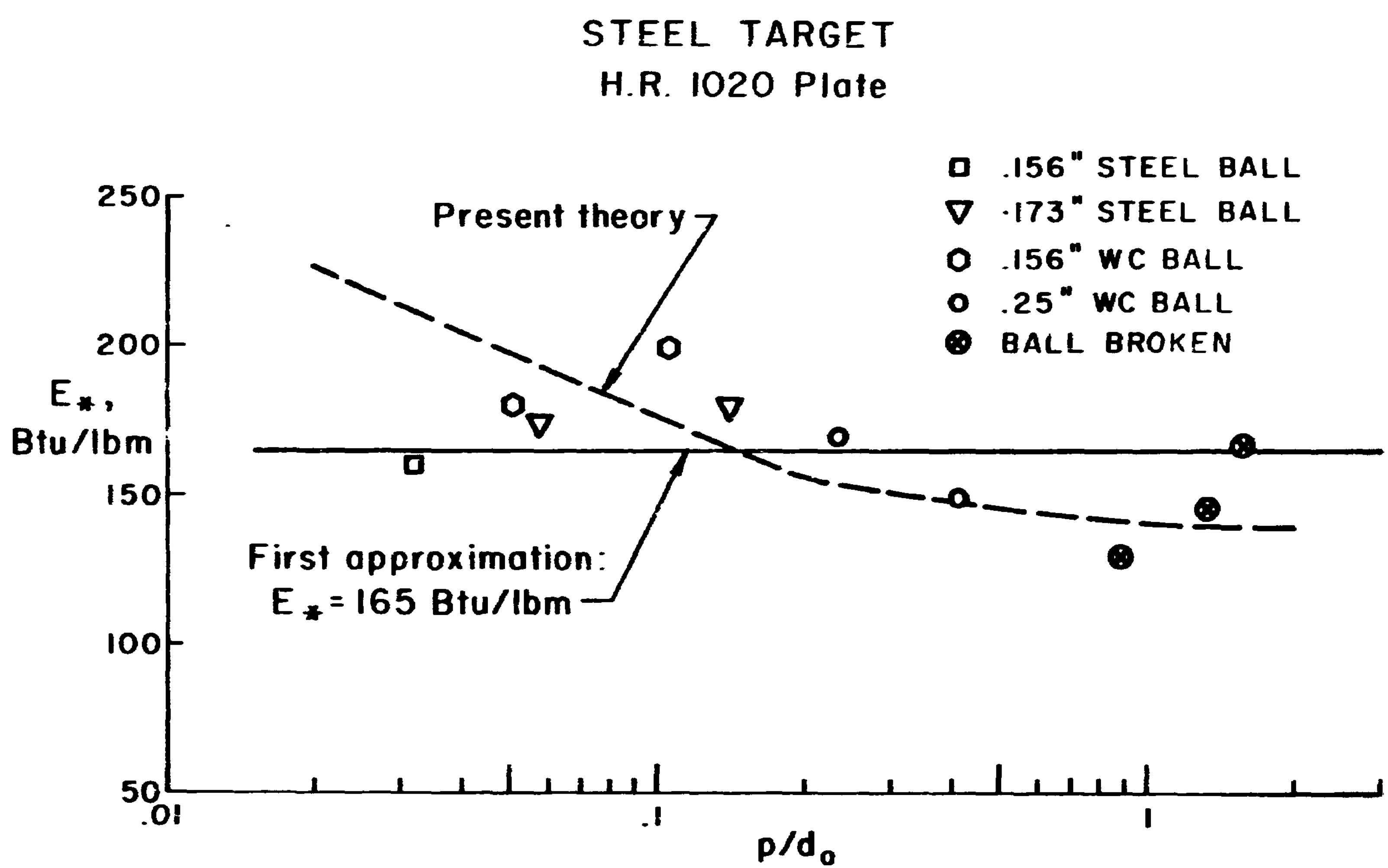
STEEL TARGET
H.R. 1020 Plate
.156" STEEL BALL
·173" STEEL BALL
.156" WC BALL
.25" WC BALL
BALL BROKEN
Present theory
First approximation:
E* = 165 Btu/lbm
E*, Btu/lbm
250
200
150
100
50
.01
.1
1
p/do

Figure 14

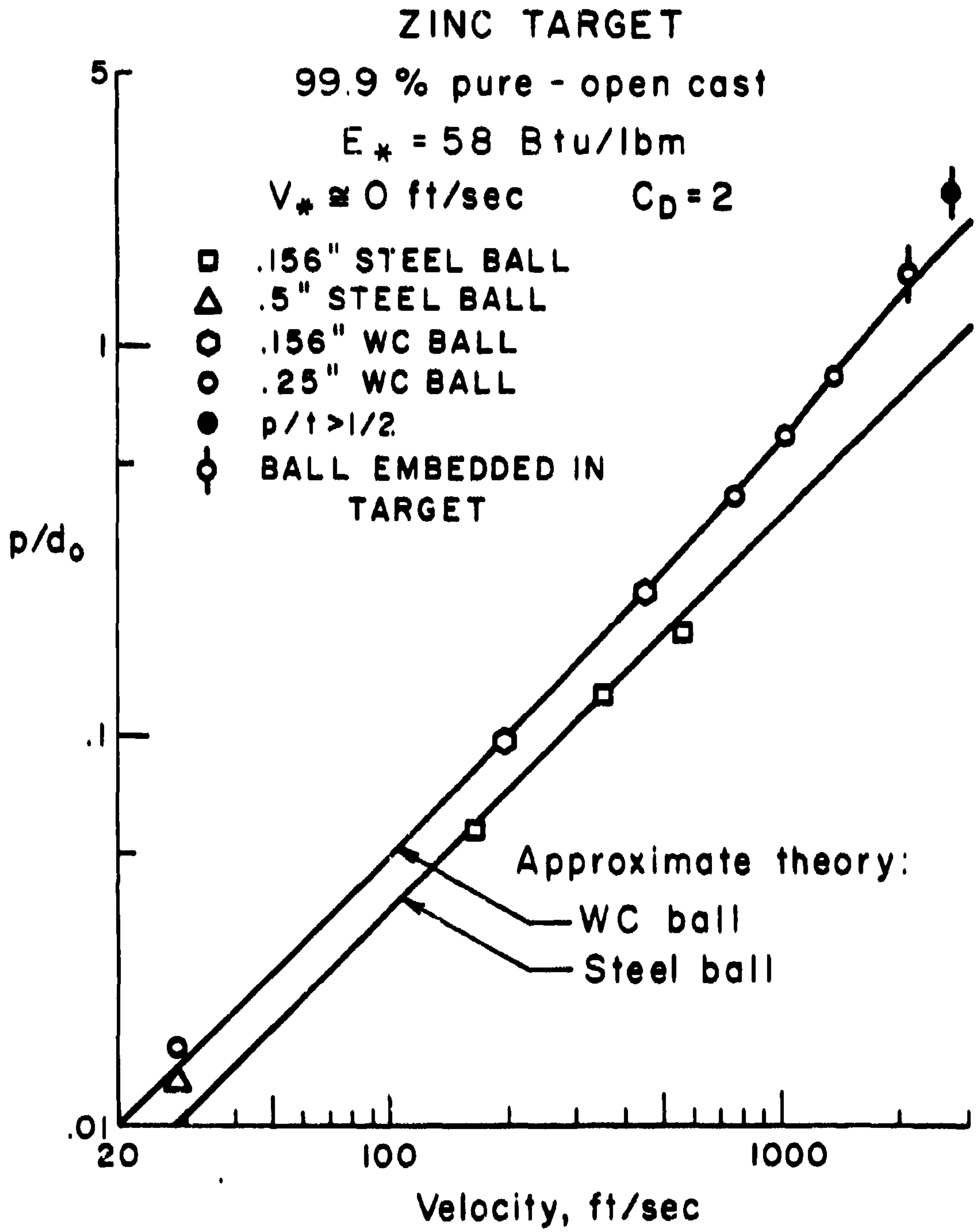
ZINC TARGET
99.9 % pure - open cast
E* = 58 Btu/lbm
V* ≅ 0 ft/sec CD = 2
.156" STEEL BALL
.5" STEEL BALL
.156" WC BALL
.25" WC BALL
p/t >1/2
BALL EMBEDDED IN TARGET
5
1
.1
.01
p/d0
20
100
1000
Velocity, ft/sec
Approximate theory:
WC ball
Steel ball

Figure 15

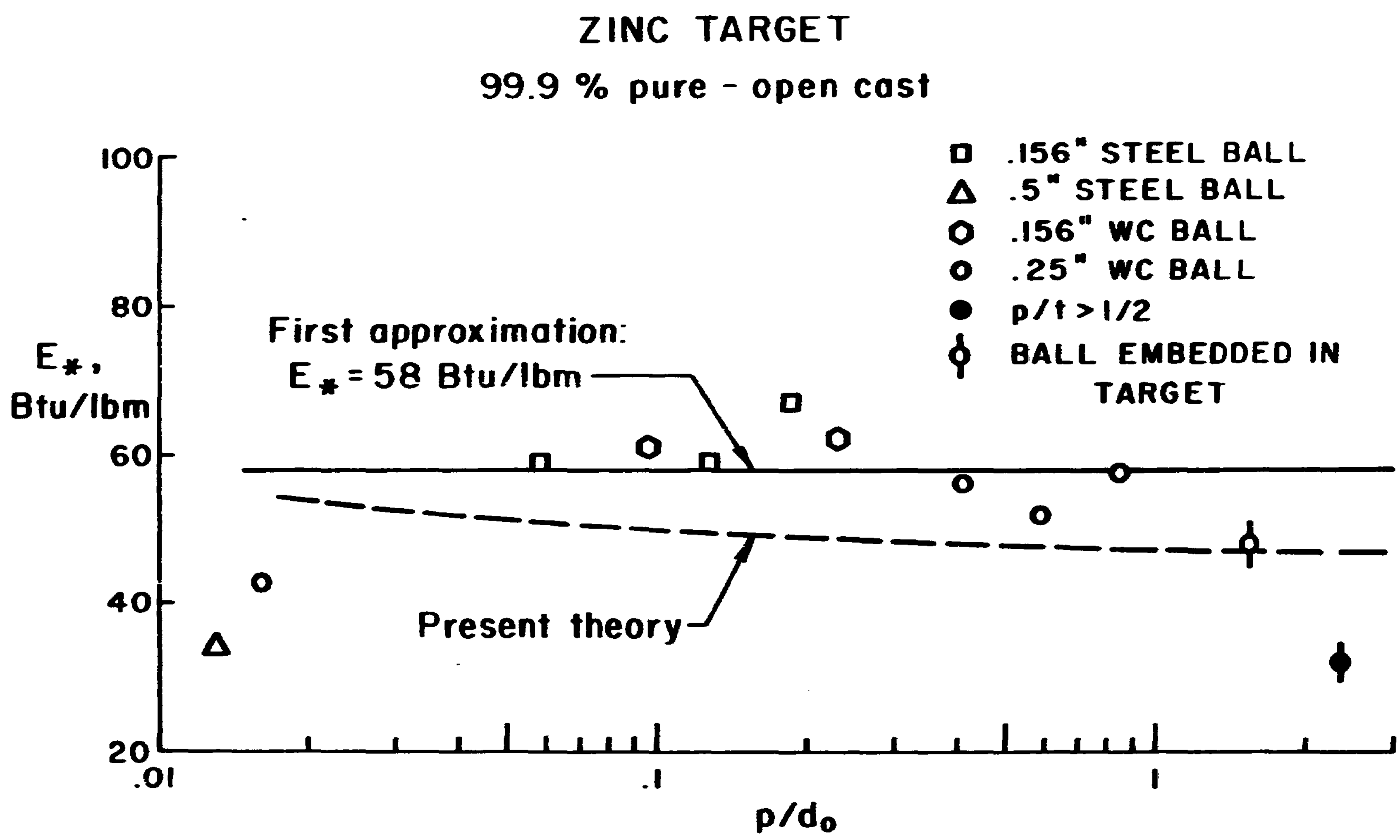
ZINC TARGET
99.9 % pure - open cast
.156" STEEL BALL
.5" STEEL BALL
.156" WC BALL
.25" WC BALL
p/t > 1/2
BALL EMBEDDED IN TARGET
First approximation:
E* = 58 Btu/lbm
Present theory
E*, Btu/lbm
100
80
60
40
20
.01
.1
1
p/d₀

Figure 16

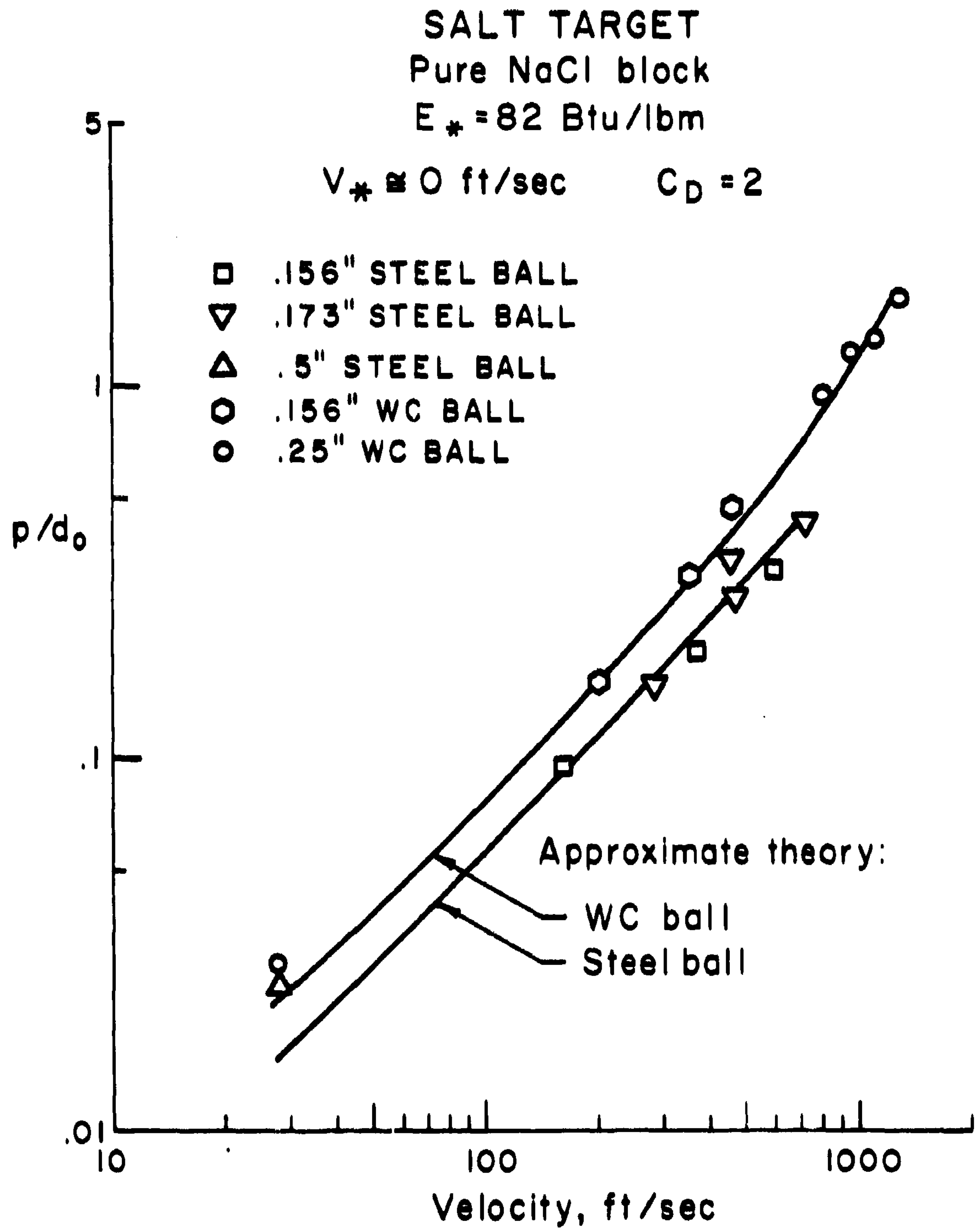
SALT TARGET
Pure NaCl block
$E_* = 82$ Btu/lbm
$V_* \cong 0$ ft/sec
$C_D = 2$
.156" STEEL BALL
.173" STEEL BALL
.5" STEEL BALL
.156" WC BALL
.25" WC BALL
p/d_0
5
1
.1
.01
10
100
1000
Velocity, ft/sec
Approximate theory:
WC ball
Steel ball

Figure 17

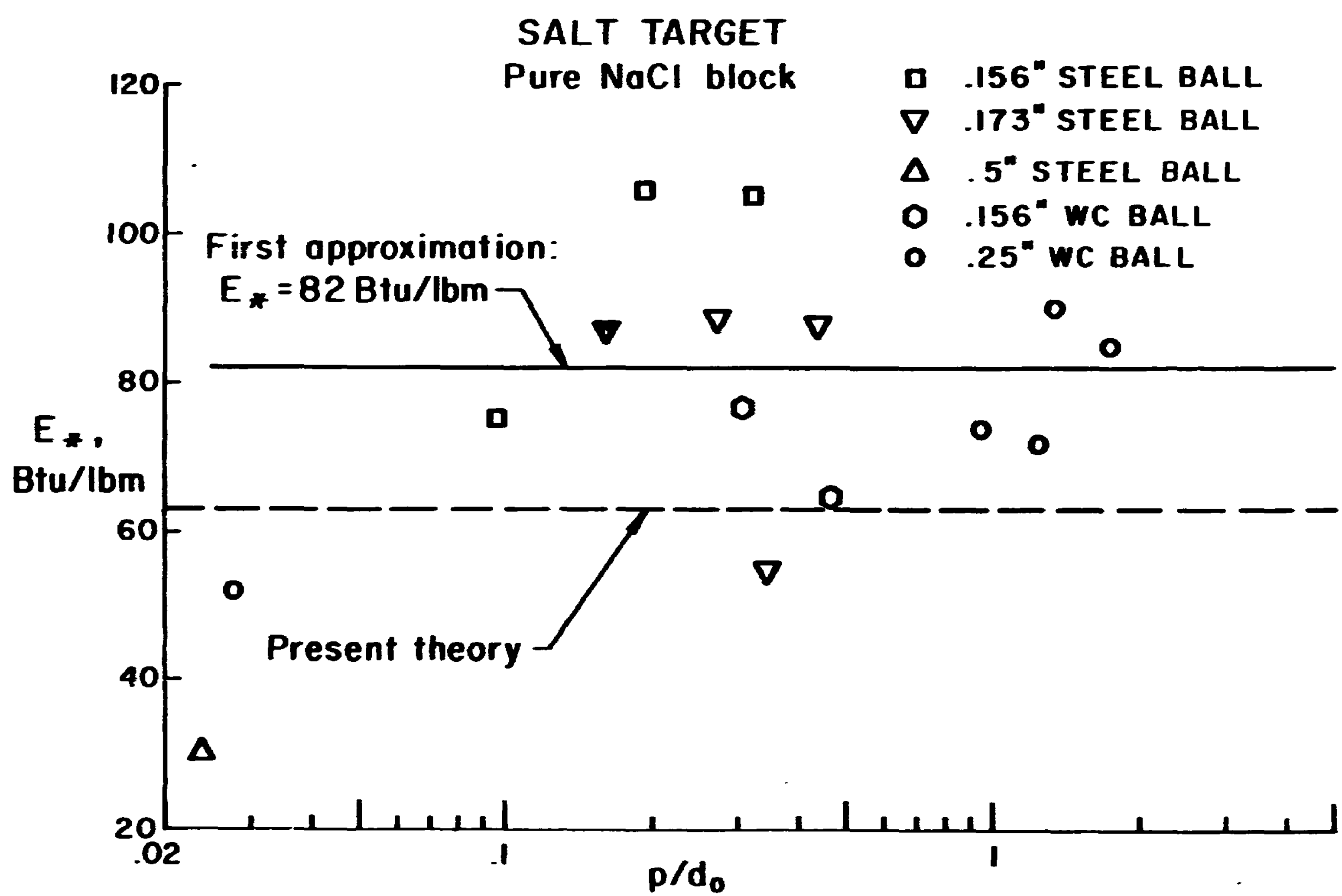
SALT TARGET
Pure NaCl block
.156" STEEL BALL
.173" STEEL BALL
.5" STEEL BALL
.156" WC BALL
.25" WC BALL
First approximation:
E* = 82 Btu/lbm
Present theory
E*, Btu/lbm
120
100
80
60
40
20
.02
.1
1
p/d0

Figure 18

TARGET MATERIAL PROPERTIES

MATERIAL	SPECIFIC GRAVITY	MELT TEMP °C	HEAT OF FUSION (BTU/LBM)	TENTATIVE VALUE E_* EXP. (BTU/LBM)	TENTATIVE VALUE E_* THEOR. (BTU/LBM)
ALUMINUM (1100F)	2.73	650	170	79	69
CADMIUM	8.81	321	24	27	26
COPPER (ETP)	9.01	1083	91	35(38)	40
IRON (CLASS 40 GRAY)	7.13	1540	117	133	137
LEAD	11.3	327	11	2.5(3.7)	4.0
STEEL (1020 H.R.)	7.86	1540	117	165	140
ZINC	7.28	421	43	58	47
POLYCARBONATE (G.E. LEXAN)	1.21	302		~130	126
SALT (NaCl)	1.99	799	223	82	63
SILICON	2.15	1435	607	~150	220
ARMOR STEEL (RHA)	7.86	1540	117		194
ARMOR ALUMINUM (5083)	2.73	650	170		196
BORON CARBIDE	2.5	2454			~1200

Table 2

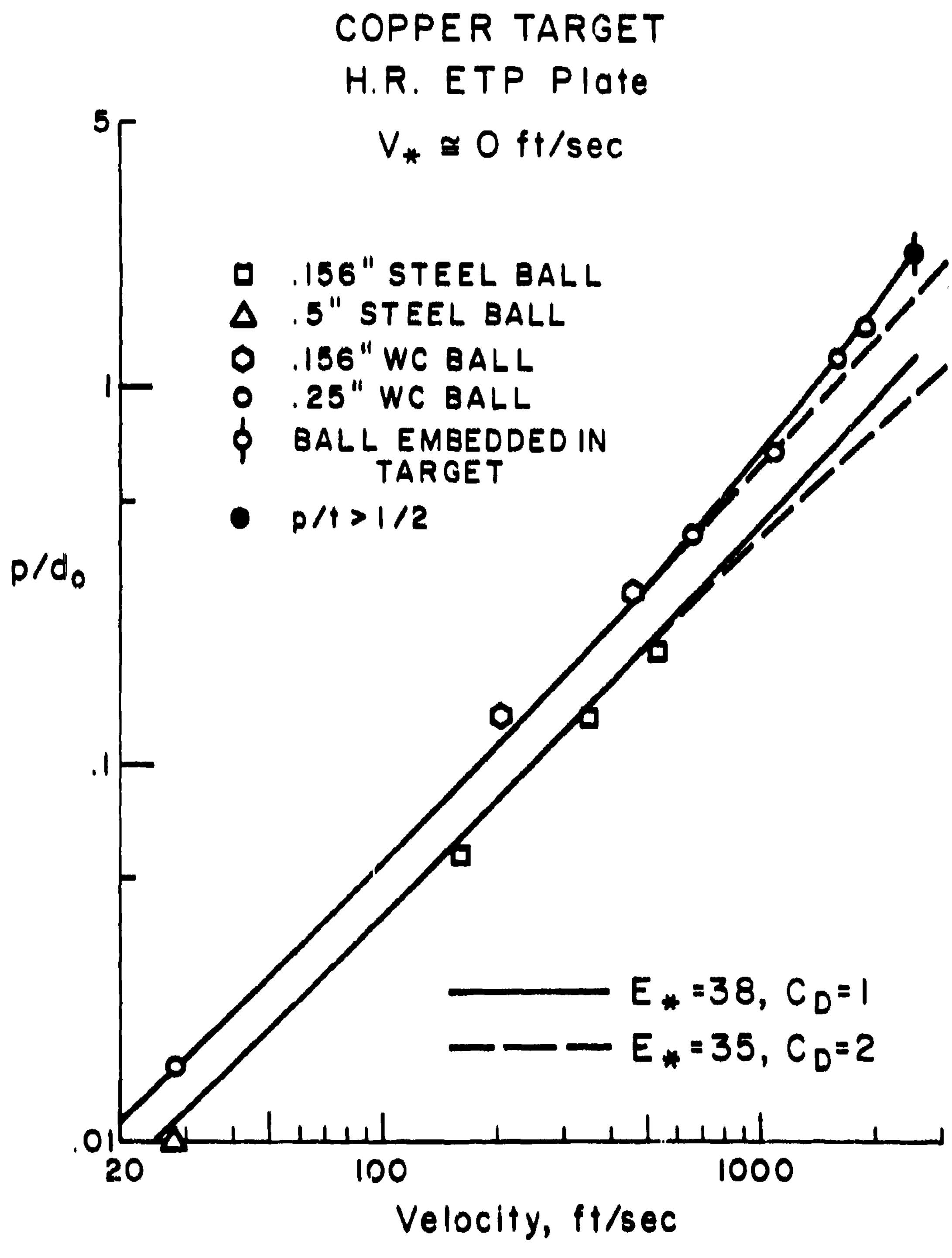
COPPER TARGET
H.R. ETP Plate
$V_* \cong 0$ ft/sec
.156" STEEL BALL
.5" STEEL BALL
.156" WC BALL
.25" WC BALL
BALL EMBEDDED IN TARGET
p/t > 1/2
p/d_0
5
1
.1
.01
20
100
1000
Velocity, ft/sec
$E_* = 38$, $C_D = 1$
$E_* = 35$, $C_D = 2$

Figure 19

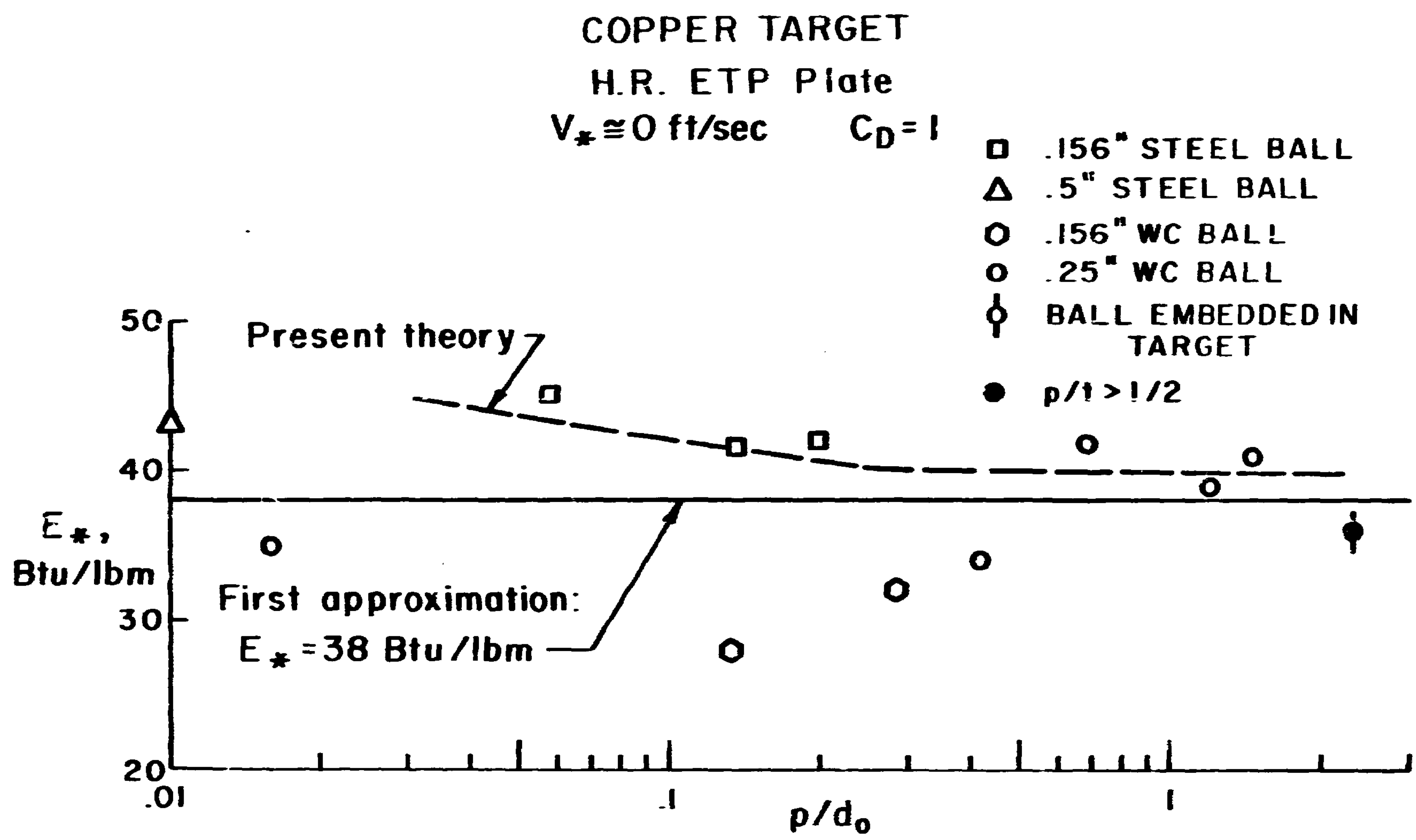
COPPER TARGET
H.R. ETP Plate
V* ≅ 0 ft/sec   C_D = 1
.156" STEEL BALL
.5" STEEL BALL
.156" WC BALL
.25" WC BALL
BALL EMBEDDED IN TARGET
p/t > 1/2
Present theory
First approximation:
E* = 38 Btu/lbm
E*, Btu/lbm
50
40
30
20
.01
.1
1
p/d_o

Figure 20

Figures 21 and 22 show the effect of C_D for lead. Again, much better correlation with data is obtained for $C_D = 1$.† In this case, the value of E_* is increased by nearly 50% with the lower value of C_D .

†The data suggest that C_D may be slightly less than 1 . There is theoretical justification for a lower value of drag coefficient. Indeed, when centrifugal force effects are included in the Newtonian pressure approximation $C_D \cong 0.75$.

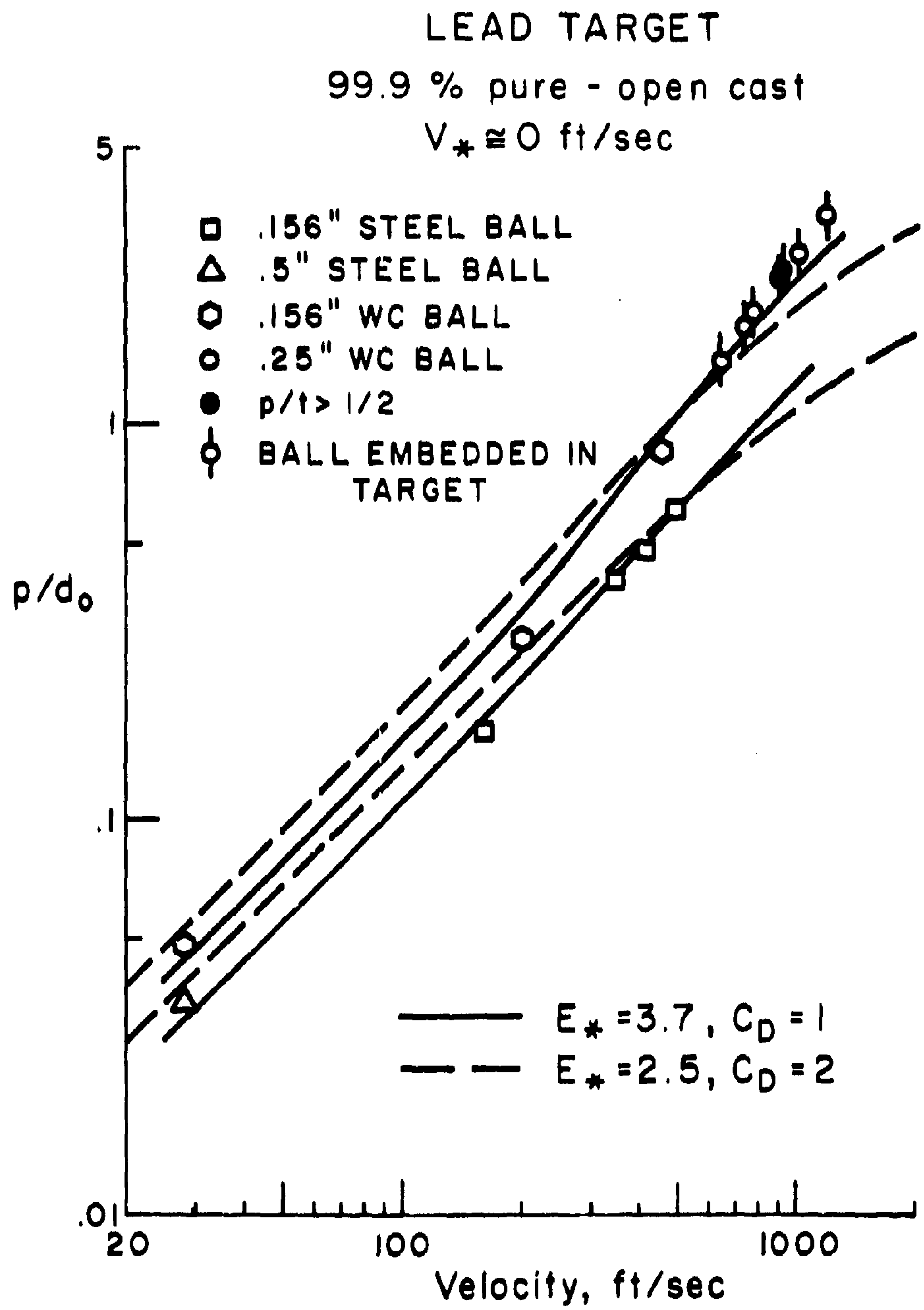

LEAD TARGET
99.9 % pure - open cast
$V_* \cong 0$ ft/sec
.156" STEEL BALL
.5" STEEL BALL
.156" WC BALL
.25" WC BALL
p/t > 1/2
BALL EMBEDDED IN TARGET
$E_* = 3.7$, $C_D = 1$
$E_* = 2.5$, $C_D = 2$
p/d_o
5
1
.1
.01
20
100
1000
Velocity, ft/sec

Figure 21

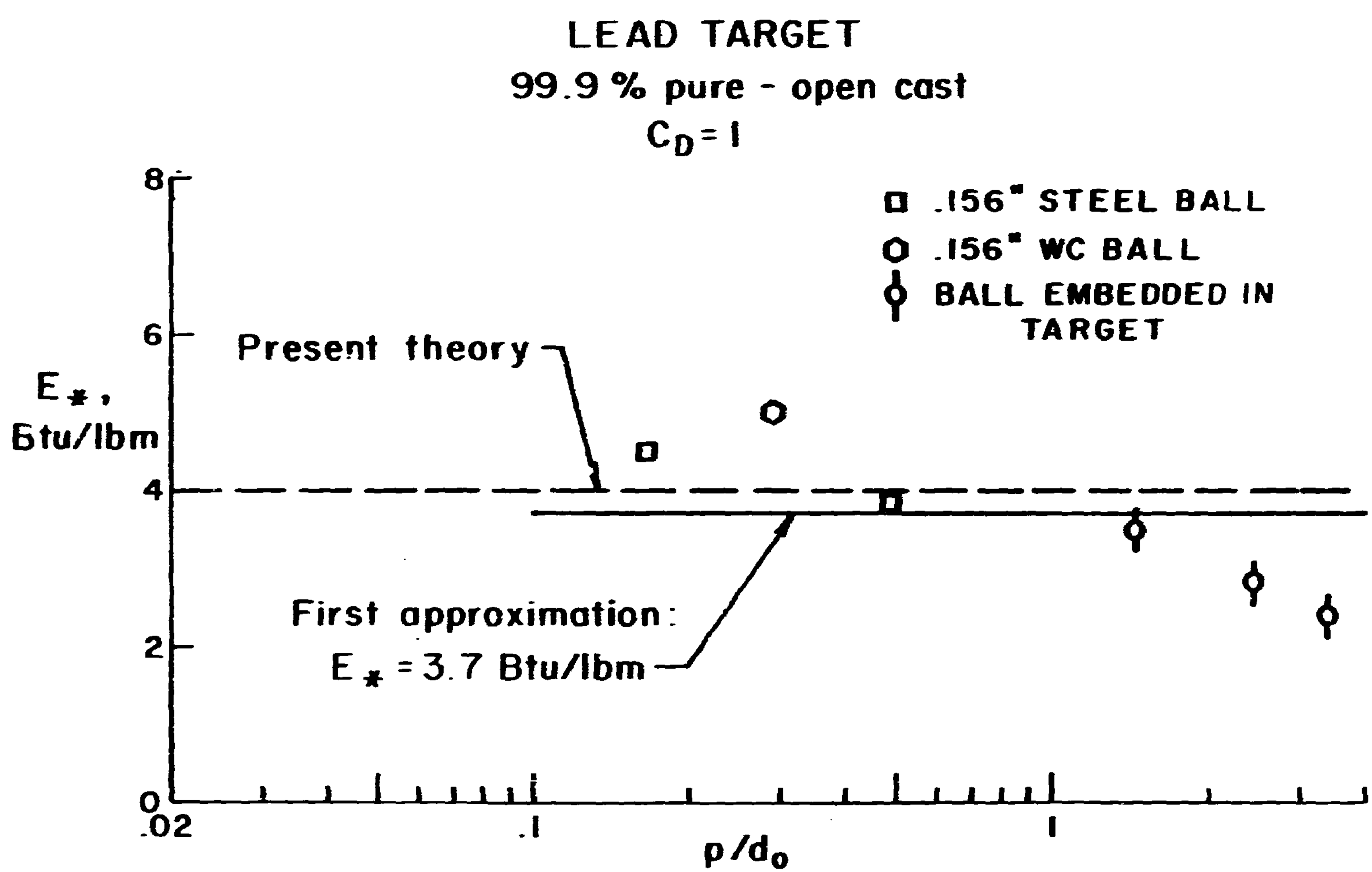

LEAD TARGET
99.9 % pure - open cast
$C_D = 1$
.156" STEEL BALL
.156" WC BALL
BALL EMBEDDED IN TARGET
Present theory
First approximation:
$E_* = 3.7$ Btu/lbm
E_*, Btu/lbm
8
6
4
2
0
.02
.1
1
p/d_o

Figure 22

CHAPTER 4

Theory for Characteristic Properties

The total initial kinetic energy of a nondeforming penetrator is absorbed by the target in three different forms (Eq. (16)). Part of the energy, given by K_{DRAG} goes into accelerating the target material as it moves around the penetrator. It is accounted for by the drag term $C_D V^2$ in the deceleration equation. This term has been discussed above. The second term, U_p, is the energy that goes into plastic deformation of the target which is rapidly dissipated as heat. The third term, U_e, accounts for the elastic or recoverable energy absorbed by the target in elastic deformation. Thus, we may write

$$\frac{1}{2} m_p V_0^2 = K_{DRAG} + U_p + U_e \tag{16}$$

Each of these terms can be predicted in advance from the hardness, Young's modulus, melting temperature and other quantities obtainable from static tests. In this section a theoretical analysis is presented leading to formulas for U_e and U_p. These formulas are then used to predict in advance the behavior of armor aluminum, armor steel, and boron carbide. First, we shall derive U_e and then derive U_p.

Theory for Elastic Energy

There are two approaches to including the elastic energy in the integral formulation of impact:

(1) The dissipative work done on the target due to drag and plastic deformation can be calculated up to the point where the penetrator velocity $V_p \lessapprox V_*$, where V_* represents the velocity of the particle at which all its remaining kinetic energy can be absorbed elastically. Then

$$\text{DEPTH OF PENETRATION} \quad p = \int_{V_o}^{V_*} V dt = -\int_{V_o}^{V_*} \frac{V m_p dV}{\rho_t \pi \left(\frac{d}{2}\right)^2 \left(\frac{C_D V^2}{2} + E_{*p}\right)} \tag{17}$$

The elastic energy then appears as an integration cutoff or an effective constant of integration.

(2) Alternatively, one can treat the elastic energy as a volume work of the same type as E_p. Then the elastic energy can be brought inside the deceleration equation:

$$m_p \dot{V} = m_p V \frac{dV}{dp} = -\rho_t \pi \left(\frac{d}{2}\right)^2 \left[E_{*p} + \frac{C_D V^2}{2} + \frac{4}{\pi d^2 \rho_t} \frac{d}{dz} U_e\right] \tag{18}$$

Since the elastic energy is a surface effect, we expect it to be a function of p/d . The velocity cutoff when integrating penetration in this case will be zero:

$$p = \int_{V_o}^{o} V dt$$

To calculate the elastic energy, assume some plastic work has already been done to produce a depression in the target of depth p (see fig. 23a). For a nondeforming ball seated in such a depression we may assume the elastic behavior of the target is linear. If r is the radius of the contact area, d the ball diameter, then a force F on the ball produces an elastic stress $F/\pi r^2$ and an elastic strain $k_1(x/r)$, where k_1 is a constant reflecting the average strain over the deformation field (fig. 23b):

$$\text{PRESSURE} = G = \frac{F}{\pi r^2} = Ek_1\left(\frac{x}{r}\right) \tag{19}$$

E is Young's modulus. k_1 shall be obtained from static tests.

The maximum elastic force F_* the target can sustain without plastic deformation is given by its Brinell hardness:

$$F_* = \pi r^2 B \tag{20}$$

assuming the contact area πr^2 doesn't change during loading.

Then the total elastic energy which can be absorbed is:

$$U_e = \frac{x_* F_*}{2} = \frac{m_p V_*^2}{2} \tag{21}$$

x_* can be obtained from (19), yielding:

$$x_* = \frac{F_*}{\pi r E k_1} \tag{22}$$

and

$$U_e = B^2 r^3 \pi / 2Ek_1 \tag{23}$$

Using the relation between contact radius r and depth p for a spherical indenter of diameter d ,

$$r = \sqrt{dp - p^2} \tag{24}$$

as well as (21), one may obtain an expression for V_*

$$V_* = \sqrt{\frac{B^2 r^3 \pi \gamma}{m_p E k_1}} = \sqrt{\frac{B^2 d^3 \pi \gamma}{m_p E k_1}} \left(\frac{p}{d}\right)^{.75} \left(1 - \frac{p}{d}\right)^{.75} \tag{25}$$

ELASTIC DEFORMATION ENERGY

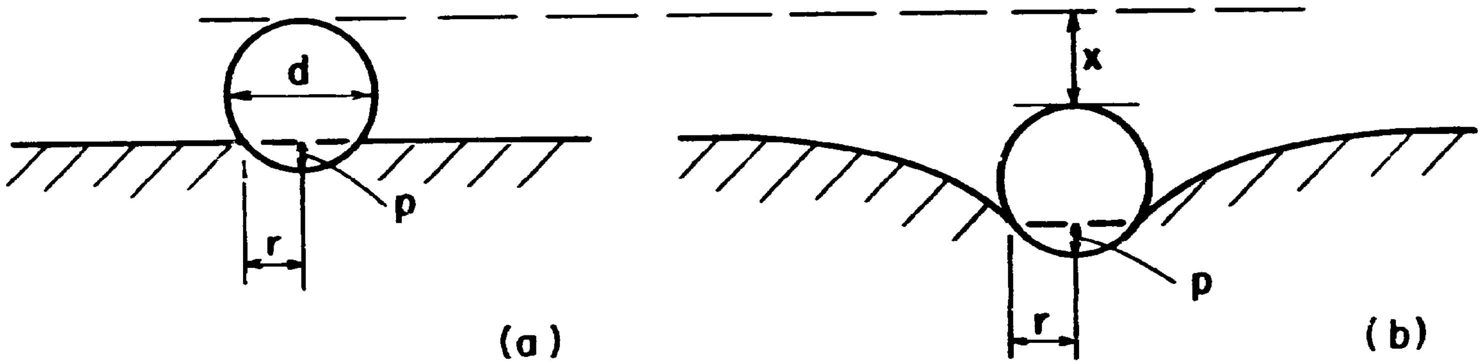

Figure 23

where k_1 is to be found from static tests. γ is the strain rate factor to account for the increase in Brinell hardness at high strain rates. The strain rate hardening of B may be obtained from the velocity-temperature relationship:

$$B(T,\dot{\varepsilon}) = B(T(1 - \beta \ln(\dot{\varepsilon}/\dot{\varepsilon}_0))) \tag{26}$$

which equates high strain rates with lower temperature, combined with the temperature dependence of B. Typically, Brinell hardness is measured at strain rates of $\dot{\varepsilon} \sim 10^{-3}$/sec, while impact tests have $\dot{\varepsilon} \sim 10^{5}$/sec. This leads to typical values for γ of 1.5 for metals and 5-10 for some plastics.

From the point of view of interpreting impact data, we have found it more convenient to convert the expression for elastic energy into an energy per volume, or energy per mass, E_{*e}, where the volume taken is that of the indentation. This is the second approach to treating the elastic energy. It is then directly comparable to E_{*p}. Using expression (23) derived above for U_e, we get:

$$E_{*e} \equiv \frac{U_e}{\rho_t(\mathrm{Vol})} = \frac{\left\{\dfrac{B^2 d^3\left(\frac{p}{d}\right)^{3/2}\left(1 - \frac{p}{d}\right)^{3/2}\gamma}{2Ek_1}\right\}}{\left\{\frac{1}{2}\, d^3 \rho_t \pi \left(\frac{p}{d}\right)^2\left(1 - \frac{2p}{3d}\right)\right\}} \tag{27}$$

where the denominator is the volume of a spherical section. This simplifies to:

$$E_{*e} = \frac{B^2\gamma}{Ek_1\rho_t}\left(\frac{p}{d}\right)^{-.5}\left\{\frac{\left(1 - \frac{p}{d}\right)^{3/2}}{\left(1 - \frac{2p}{3d}\right)}\right\} \tag{28}$$

In order to obtain the parameter k_1 of the elastic deformation field and to check the predicted (p/d) dependence of V_* and E_{*e} empirically, we have carried out a series of static tests. Using a Hounsfield tensometer, which is capable of applying up to a 2-ton compressive load, a tungsten carbide ball was pressed into several target materials and the elastic energy U_e measured by the following technique:

(1) Indent target to depth p using tungsten carbide ball and Hounsfield tensometer at some load G.

(2) Back out ball and measure depth p.

(3) Reinsert ball, reapply compressional load slowly, measuring distance of travel on vernier micrometer.

(4) Periodically back out ball and check depth to make sure it hasn't increased.

(5) Measure maximum force which can be applied without producing additional plastic deformation. This is F_* .

(6) The corresponding length of travel of ball is x_* .

(7)
$$U_e = \frac{F_* x_*}{2}$$

Using the value of U_e obtained by this technique, we may obtain values for V_* and E_{*e} from the static tests using the expressions:

$$V_* = \sqrt{\frac{2\gamma U_e}{m_p}}$$

$$E_{*e} = \frac{\gamma U_e}{\rho_t (Vol)} \qquad (29)$$

where γ is the strain rate factor introduced above.

The empirical values of V_* obtained in this manner are displayed in figure 24 for Lexan, rolled homogeneous armor steel, armor aluminum, soft aluminum and lead. From static tests, we can fit our results for all materials to:

$$V_* \cong k_2\left(\frac{p}{d}\right)^{.6} \qquad (30)$$

where k_2 is different for each material. A summary of results for a wide variety of materials is shown in figure 25.

The static test results summarized in the figure lead immediately to one prediction for the dynamic impact tests. One of our dynamic tests consisted of dropping a .250-inch WC ball on a target from a height of 14 ft to obtain a low velocity impact data point. If this impact, which we call the "Rafter Drop Experiment," produced a hole .001-inch deep or greater, which was the limit of measurement sensitivity, corresponding to $p/d \geq .004$, then we concluded that the target had been damaged. The impact velocity corresponding to a 14-ft height is 28 ft/sec. Referring to figure 25, we draw a vertical line at $p/d = .004$. One would predict that any material whose V_* is greater than 28 ft/sec at this p/d should show no damage, because the energy could all be absorbed elastically. The plastic work done at this p/d is negligible. Any material with $V_* < 28$ ft/sec at $p/d = .004$, we would predict should show surface damage at least one mil deep. This is what was found experimentally. The lead, soft aluminum, zinc and armor aluminum showed surface damage in the rafter drop. The steels and Lexan did not. The cast iron showed marginal damage in the rafter drop, as would be expected from its V_* of 28 ft/sec at $p/d = .004$.

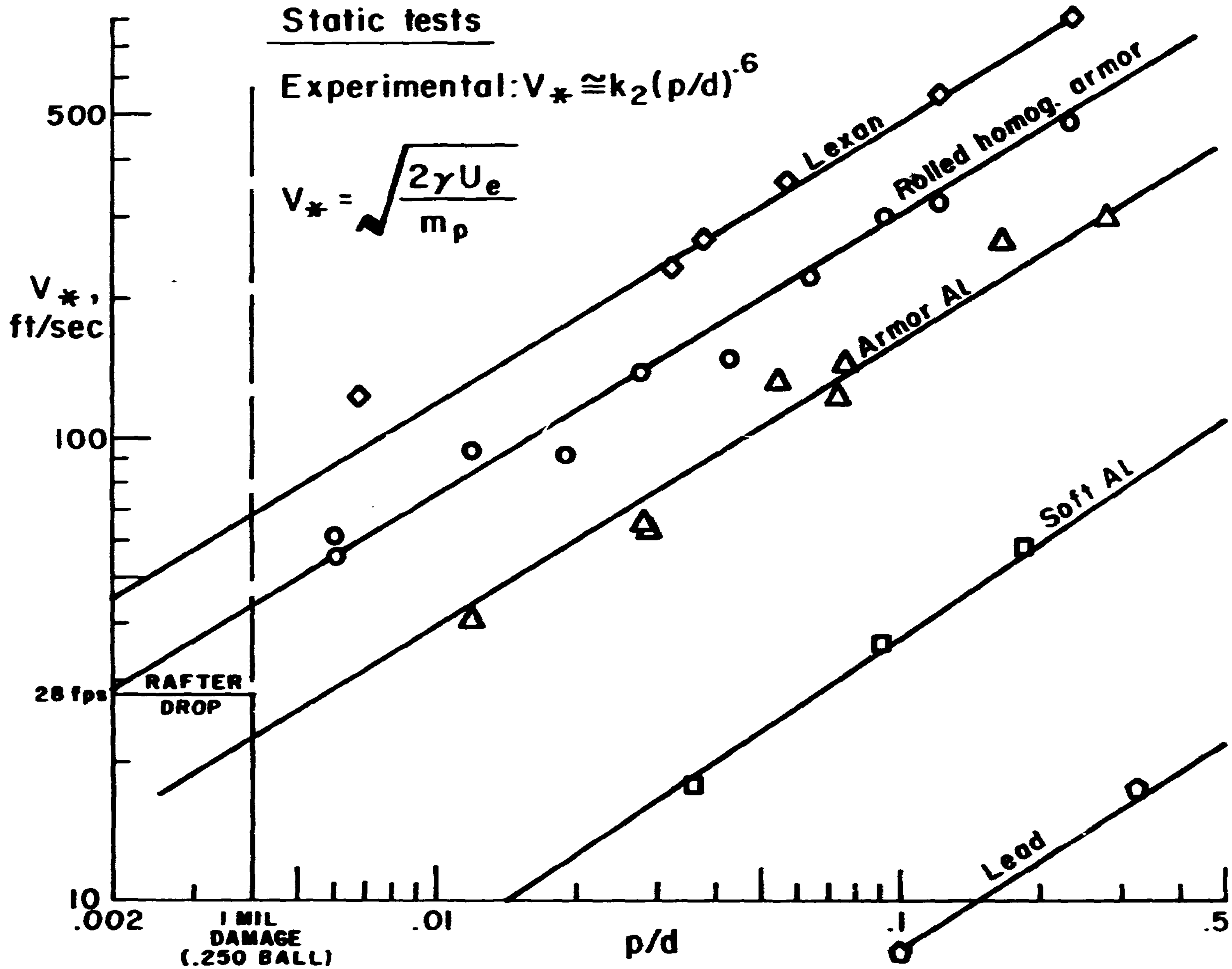
Static tests
Experimental: $V_* \cong k_2 (p/d)^{.6}$
$V_* = \sqrt{\frac{2\gamma U_e}{m_p}}$
V_*, ft/sec
500
100
28 fps
10
RAFTER DROP
.002
1 MIL DAMAGE (.250 BALL)
.01
.1
.5
p/d
Lexan
Rolled homog. armor
Armor Al
Soft Al
Lead

Figure 24

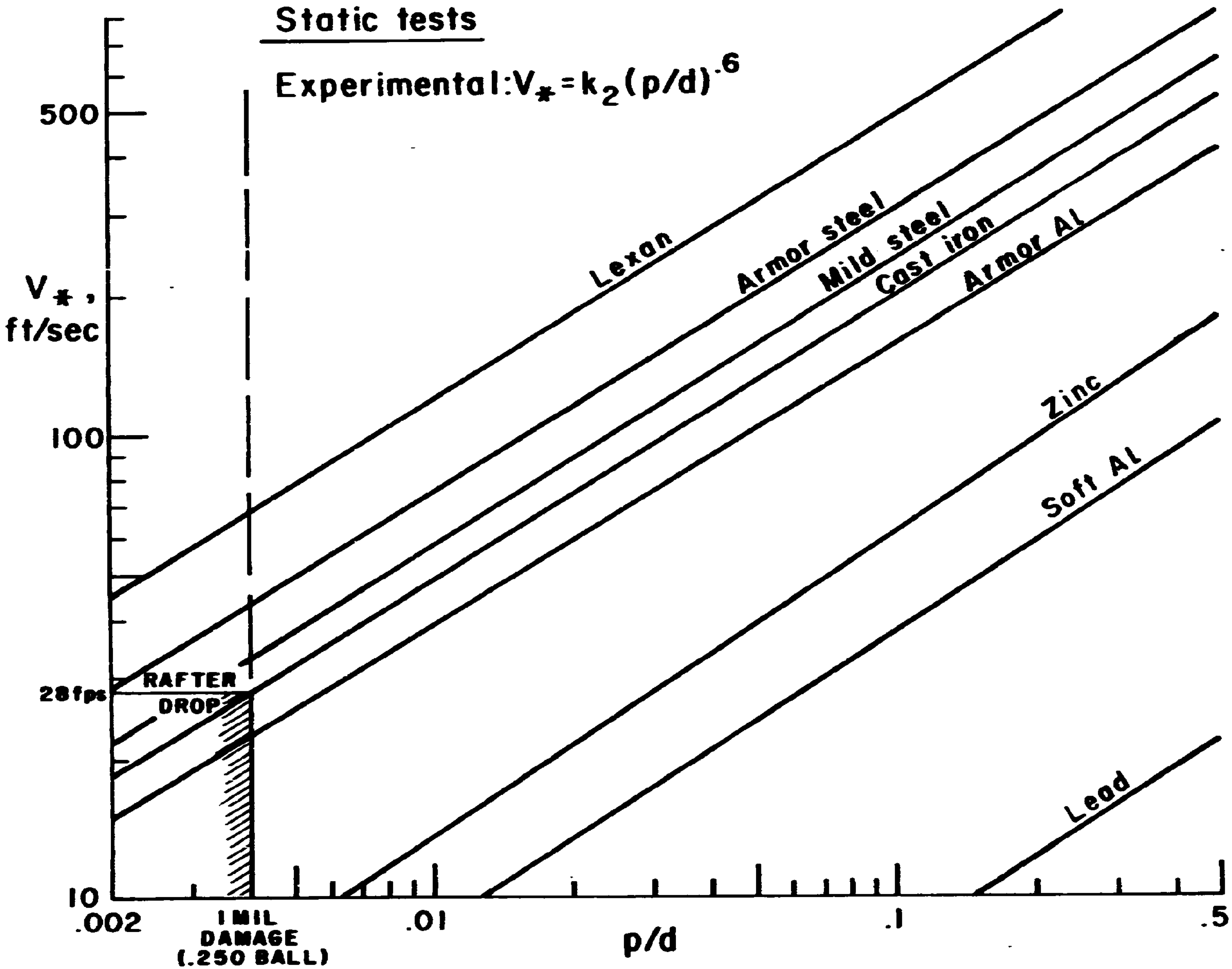
Static tests
Experimental: $V_* = k_2 (p/d)^{.6}$
V_*, ft/sec
500
100
28fps
10
RAFTER
DROP
Lexan
Armor steel
Mild steel
Cast iron
Armor Al
Zinc
Soft Al
Lead
.002
1 MIL
DAMAGE
(.250 BALL)
.01
.1
.5
p/d

Figure 25

When the static test results are converted into values for E_{*e}, the curves of figure 26 are obtained. Lexan, which has a low density and high elastic energy, has a very large E_{*e} compared to the metals. E_{*e} was found from static tests to be well described for all materials by:

$$E_{*e} = k_3\left(\frac{p}{d}\right)^{-.75} \tag{31}$$

where k_3 is a different constant for each material.

We summarize our results in the following way:

<u>Experimental (From Static Tests)</u>

$$V_* = k_2\left(\frac{p}{d}\right)^{.6}$$

$$E_{*e} = k_3\left(\frac{p}{d}\right)^{-.75}$$

<u>Theoretical</u>

$$V_* = \sqrt{\frac{B^2 d^3 \pi\gamma}{m_p E k_1}}\left(\frac{p}{d}\right)^{.75}\left(1 - \frac{p}{d}\right)^{.75}$$

$$E_{*e} = \frac{B^2\gamma}{E k_1 \rho_t}\left(\frac{p}{d}\right)^{-.5}\left(\frac{\left(1 - \frac{p}{d}\right)^{3/2}}{\left(1 - \frac{2p}{3d}\right)}\right)$$

Experimentally, we found $V_* \sim (p/d)^{.6}$, while theoretically we would have expected roughly: $V_* \sim (p/d)^{.75}$. The additional term $(1 - p/d)^{.75}$ will have the effect of reducing the exponent somewhat, but the discrepancy in exponents probably is due to our assumption that the contact area does not increase as force is applied to the ball.

Similarly, for E_{*e} the experimental value is $(p/d)^{-.75}$, while theoretically it was predicted that $E_{*e} \sim (p/d)^{-.5}$. The approximate agreement of the expressions and the exponents leads us to believe we understand the mechanism of elastic energy.

We find from the static tests that a value for k_1 of 0.62 provides a good fit to all the data. Using the empirical (p/d) dependence and incorporating the theoretical coefficients, we synthesize the following formulas for V_* and E_{*e}.

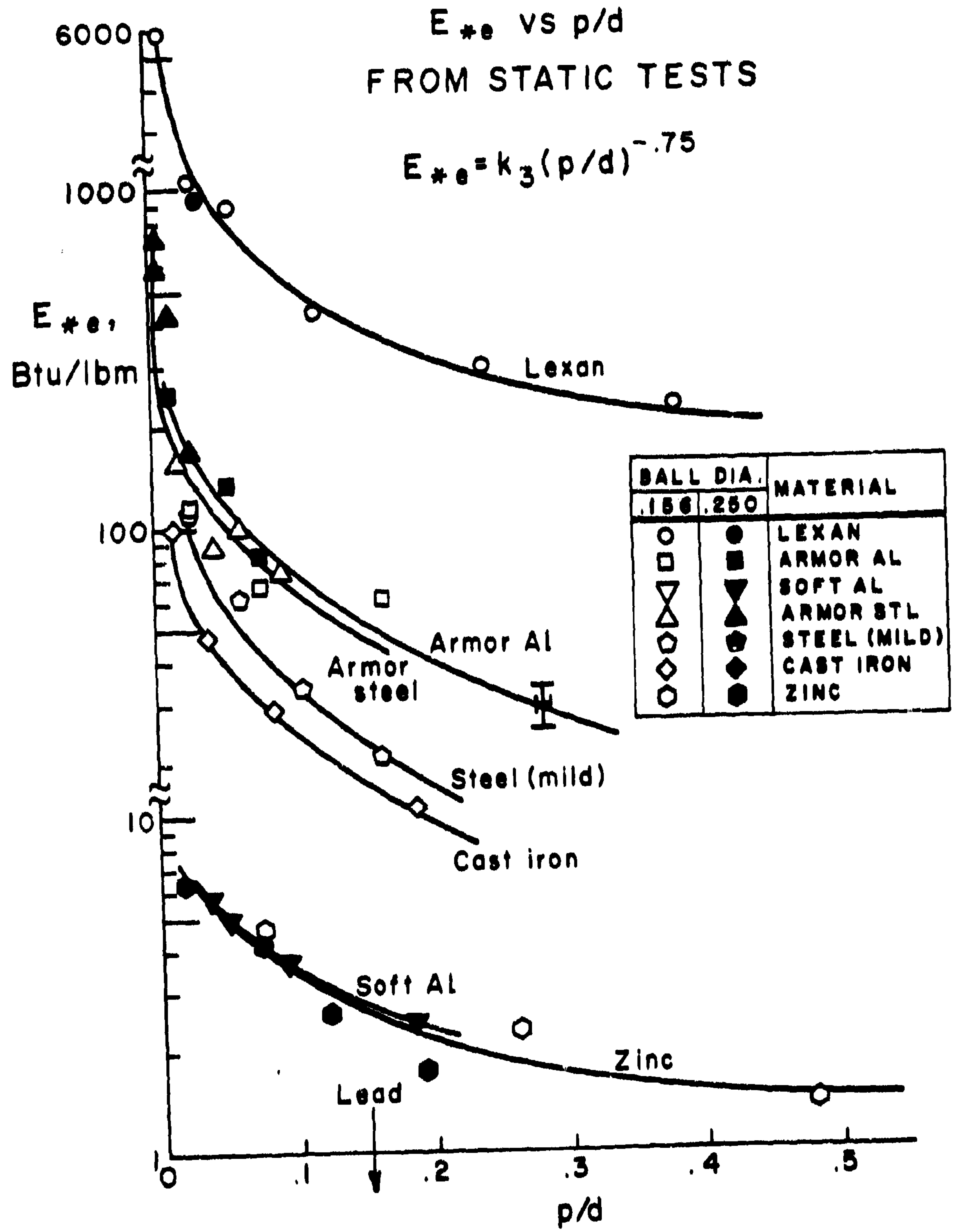

E*e VS p/d
FROM STATIC TESTS
E*e=k3(p/d)^-.75
6000
1000
100
10
1
E*e,
Btu/lbm
Lexan
Armor Al
Armor steel
Steel (mild)
Cast iron
Soft Al
Zinc
Lead
0
.1
.2
.3
.4
.5
p/d
BALL DIA.
.156
.250
MATERIAL
LEXAN
ARMOR AL
SOFT AL
ARMOR STL
STEEL (MILD)
CAST IRON
ZINC

Figure 26

Theoretical (Synthesis)

$$V_* = 3.3 \sqrt{\frac{B^2 \pi d^3 \gamma}{m_p E(.62)}} \left(\frac{p}{d}\right)^{.6} \tag{32}$$

$$E_{*e} = 1.09 \cdot 10^{-3} \frac{B^2 \gamma}{\rho_t E} \left(\frac{p}{d}\right)^{-.75} \tag{33}$$

where B is Brinell hardness in Nt/m^2 , E is Young's modulus in Nt/m^2 , ρ_t is the target density in kg/m^3 , m_p is the penetrator mass in kg , E_{*e} is given in BTU/lbm, V_* in ft/sec.

In figure 27 the theoretical values of the constant coefficients are compared to the values found in static tests. The theoretical expression shows good rough agreement for a wide range of materials. We conclude that if one cannot perform the static tests in advance to measure k_2 and k_3 , the expressions in equations (32) and (33) will provide a good approximation.

As an illustration of the importance of E_{*e} for some materials, refer to the data for Lexan in figure 28. The E_* obtained in high speed impact tests was found not to be constant, but to become very large at low p/d . The solid line, which is the predicted E_* from static tests, and which goes as $(p/d)^{-.75}$ for small p/d , fits the data very well. We conclude that for Lexan the elastic energy is comparable to the plastic work for p/d as large as 2. Thus, for highly elastic materials, E_{*e} can dominate E_{*p} .

Theory for the Plastic Energy E_{*p}

The plastic deformation work performed on the target is described by E_{*p} . The plastic deformation may be thought of as analogous to a Brinell Hardness Experiment (see figure 29a). As the particle moves through the material there will be a pressure on the front face which is $F/\pi r^2$ where r is the contact radius. The force F arises because the particle does work in the volume around it by shearing the target material and causing it to flow. The work done on each small region of target material is just the flow stress σ_F times the distance it moves, so the total work per deformation volume is proportional to the flow stress σ_F . Using the well known Prandtl solution to the deformation flow field one finds:

$$\frac{F}{\pi r^2} = B = 3.1\sigma_F = \left\langle \frac{\text{WORK}}{\text{VOLUME}} \right\rangle \tag{34}$$

where B is the Brinell hardness. Since E_{*p} is also a measure of the plastic shear work per volume done by a penetrator, we take:

$$E_{*p} = \frac{C_2 \sigma_F(T,\dot{\varepsilon})}{\rho_t} = \frac{C_3 B(T,\dot{\varepsilon})}{\rho_t} \tag{35}$$

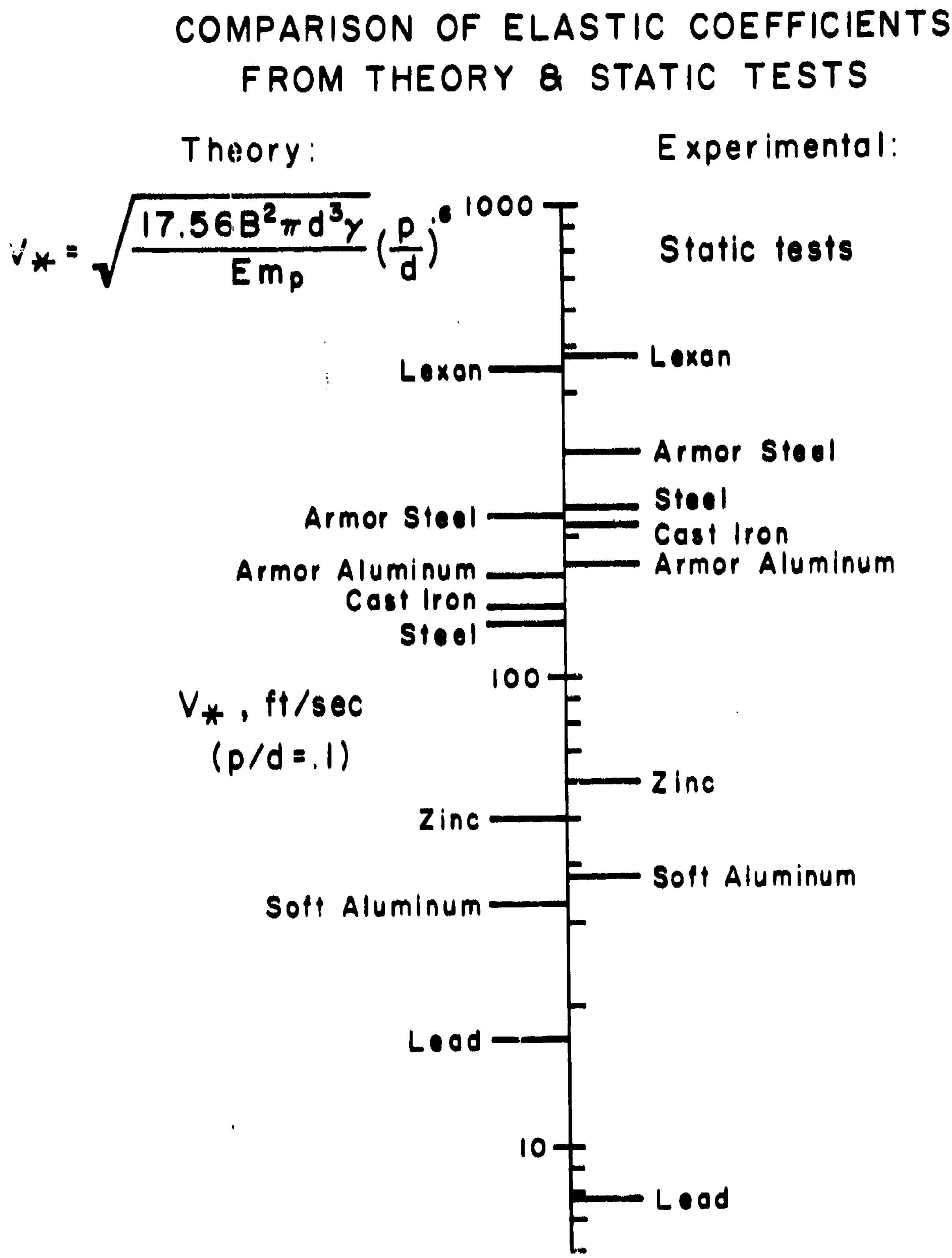
COMPARISON OF ELASTIC COEFFICIENTS
FROM THEORY & STATIC TESTS
Theory:
Experimental:
$V_* = \sqrt{\frac{17.56 B^2 \pi d^3 \gamma}{E m_p}} \left(\frac{p}{d}\right)^{.6}$
Static tests
1000
100
10
Lexan
Lexan
Armor Steel
Steel
Cast Iron
Armor Aluminum
Armor Steel
Armor Aluminum
Cast Iron
Steel
V_*, ft/sec
(p/d=.1)
Zinc
Zinc
Soft Aluminum
Soft Aluminum
Lead
Lead

Figure 27

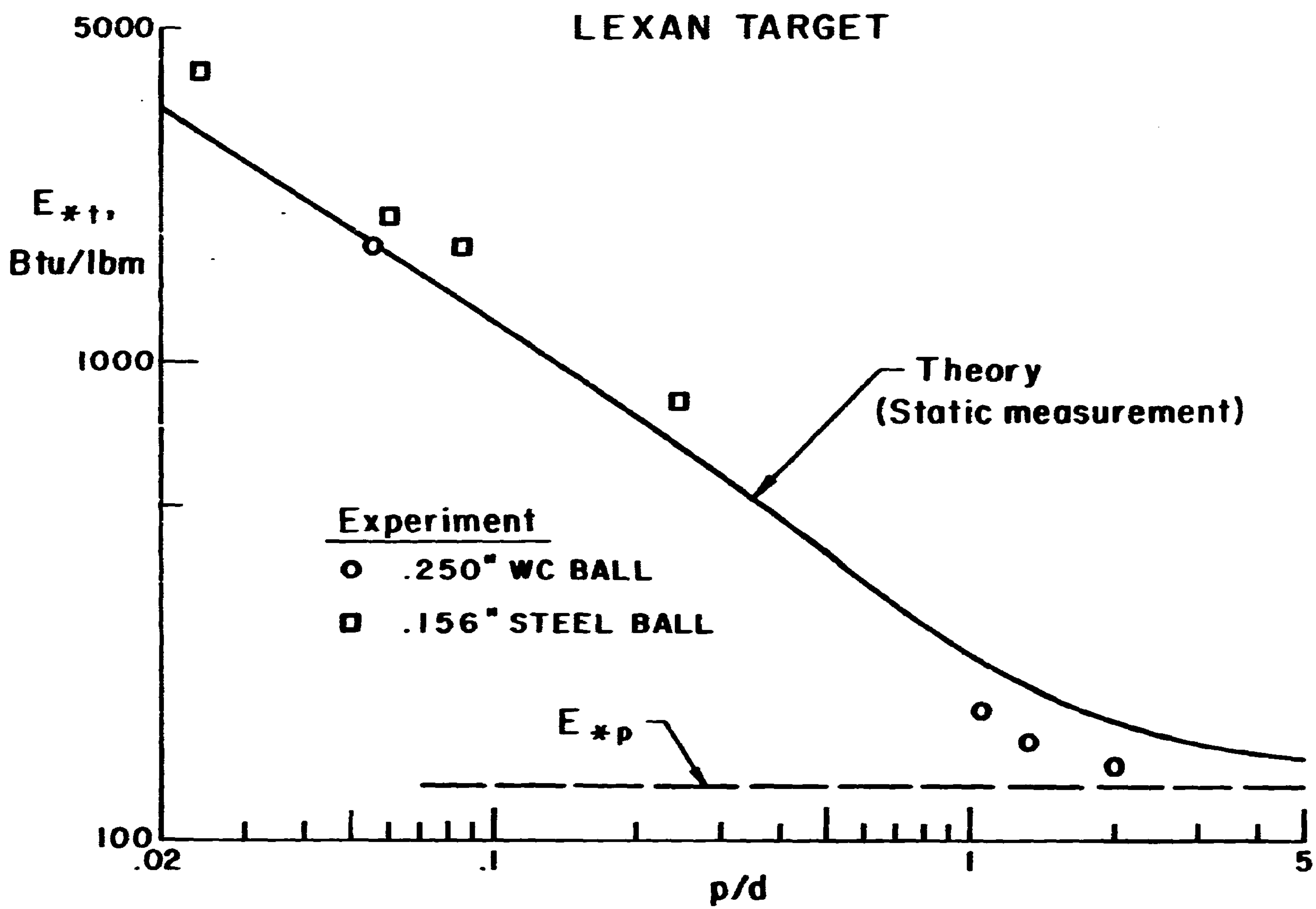
LEXAN TARGET
5000
1000
100
E*t, Btu/lbm
.02
.1
1
5
p/d
Theory
(Static measurement)
Experiment
.250" WC BALL
.156" STEEL BALL
E*p

Figure 28

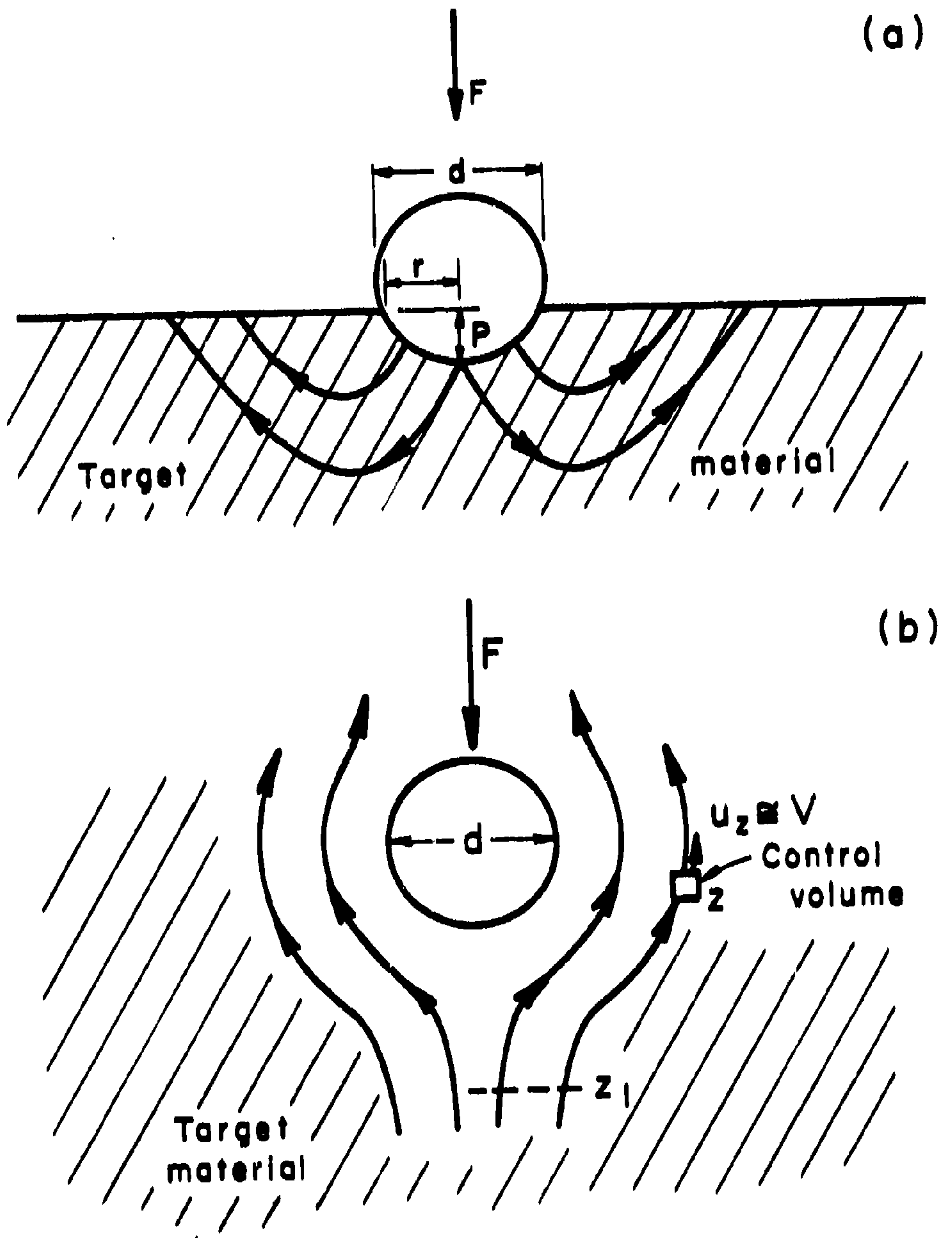

(a)
F
d
r
P
Target
material
(b)
F
d
$u_z \cong V$
Control volume
z
z_1
Target material

Figure 29

where ρ_t is the density of the target material and σ_F is the measured flow stress at temperature T and strain rate $\dot{\varepsilon}$ of the experiment.

It has been found experimentally and there is theoretical basis for this finding that the constant temperature flow stress σ_F may be written:

$$\sigma_F(T,\dot{\varepsilon}) = \sigma_F\left[T(1 - \beta \ln(\dot{\varepsilon}/\dot{\varepsilon}_o))\right] \tag{36}$$

This result comes from the well-known "velocity-temperature" or "temperature-strain rate" interrelationship. The import of the formula is that a hardness test done at a higher strain rate (assuming no heating effects) will be equivalent to one done at lower temperature. β is typically .018 and $\dot{\varepsilon}_o = 10^{-3}$/sec, where T is expressed in ^oK.

At the very high strain rates of impact the heat dissipated in the material by the flow work cannot be conducted away fast enough to allow one to use ordinary Brinell hardness tests to evaluate E_*. A Brinell hardness experiment is low enough so any heat generated has time to diffuse, so all the material remains at one temperature; but, in an impact test, the high strain rates of shear near the penetrator can cause large local temperature rises and these will in turn change the flow stress σ_F in those regions.

To account for this phenomenon when using Eq. (35) we must solve for the temperature rise caused by the flow work. The equation for this is

$$\rho_t C_p \frac{\partial T}{\partial t} = \alpha_\rho T \frac{\partial p}{\partial t} + \kappa \nabla^2 T + \sigma_{ij} \frac{\partial u_i}{\partial x_j} \tag{37}$$

where the total stress π_{ij} is

$$\pi_{ij} = -p\delta_{ij} + \sigma_{ij}$$

and α_ρ is the bulk coefficient of thermal expansion. This equation describes the temperature rise in a small control volume of target material (see figure 29b) as it passes around the penetrator. C_p is the heat capacity of the target material. The first term on the right accounts for adiabatic compressional heating of the control volume, $\kappa \nabla^2 T$ accounts for any heat flow into or out of the volume, and the last term expresses the shear heating of the small volume of material.

Now we shall argue that for our impact experiments the first two terms on the right-hand side may be neglected compared to the third term. The third term, which is the flow stress times shear strain rate is:

$$\sigma_{ij} \frac{\partial u_i}{\partial x_j} = O\left(\sigma_F \frac{V}{a}\right) \tag{38}$$

where a is the radius of the penetrator and V its velocity. The adiabatic compressional term is just $\alpha_\rho T$ times the change of pressure with time which is:

$$\alpha_\rho T \frac{\partial p}{\partial t} = 0\left[\alpha_\rho T \frac{V}{a} (\sigma_F + \rho V^2)\right] \qquad (39)$$

For the range of impact velocities of interest, $\rho V^2 \lesssim \sigma_F$. In addition, $\alpha_\rho \sim 10^{-5}/°C$ and $T \sim 10^{+3}/°C$ so:

$$\alpha_\rho T \frac{\partial p}{\partial t} = 0\left[10^{-2}\sigma_F \frac{V}{a}\right]$$

and is therefore negligible relative to the shear heating.† And, finally,

$$\kappa \nabla^2 T = 0\left(\frac{\kappa T}{a^2}\right)$$

For materials where the strain rates are so high that:

$$\sigma_F \frac{V}{a} >> \frac{\kappa T}{a^2}$$

a simple theory may be developed. For example, in the case of copper, which has a very large κ, $\frac{\kappa T}{a^2} = 10^{-2} \sigma_F \frac{V}{a}$ for typical impact tests. Equation (22) may then be written:

$$\rho C_p \frac{\partial T}{\partial t} \sim \sigma_F \frac{V}{a}$$

or

$$\rho C_p dT \cong f_1 \sigma_F \frac{dz}{a} \qquad (40)$$

where z measures the distance traversed by a material element, as in figure 29b.

We assume that the temperature dependence of the flow stress can be described by:

$$\sigma_F(T) = \sigma_F(T_o) e^{-\left(\frac{T-T_o}{\alpha_1 T_m}\right)} = \sigma_{F_o} e^{-\left(\frac{T-T_o}{\alpha_1 T_m}\right)} \qquad (41)$$

---

†At high velocities, $\sim V_{SOUND}$ in the target, compressional heating will become important, since in this region $\rho V^2 >> \sigma_F$. When $V = V_{SOUND}$, then $\rho V^2 \sim E \sim 10^2 \sigma_F$, or $\alpha_\rho T \frac{\partial p}{\partial t} \sim \sigma_F \frac{V}{a}$.

This is in good agreement for all materials, where T_m is the melting temperature and $\alpha \lessapprox \alpha_1 \lessapprox .4$. Then Eq. (40) can be written

$$\rho C_p dT = f_1 \sigma_F(T_1, \dot{\varepsilon}) e^{-\left(\frac{T-T_o}{\alpha_1 T_m}\right)} \frac{dz}{a} \tag{42}$$

This may be integrated to give

$$\sigma(z) = \left(\frac{1}{\sigma_F(T_1, \dot{\varepsilon})} + \frac{f_1}{\alpha_1 \rho C_p T_m} \frac{z}{a}\right)^{-1} \tag{43}$$

As the volume of target material progresses a distance z along its flow path, the local flow stress decreases according to this relation.

The average level of flow stress in the deforming medium in the vicinity of the penetrator can be written

$$\langle\sigma_F\rangle = \frac{1}{(z_2 - z_1)} \int_{z_1}^{z_2} \frac{dz}{\left(\frac{f_1}{\alpha_1 \rho C_p T_m}\right)\frac{z}{a} + \frac{1}{\sigma_F(T_1, \dot{\varepsilon})}} \tag{44}$$

which is the volume average of σ_F . If $(z_2 - z_1)$ is taken equal to $f_2 a$, where a is the ball radius, then:

$$\langle\sigma_F\rangle = \frac{\alpha_1}{f_1 f_2} \rho C_p T_m \ln\left(\frac{f_1 f_2}{\alpha_1} \cdot \frac{\sigma_F(T_1 \dot{\varepsilon})}{\rho C_p T_m} + 1\right) \tag{45}$$

Note that $\langle\sigma_F\rangle$ only really depends on one parameter:

$$\frac{\alpha_1}{f_1 f_2} = \alpha \tag{46}$$

and the measurable static properties of the material, using Eq. (36) to account for strain rate.

We reason that α is roughly a constant for the following reasons:

1. α_1 does not vary too much $(.2 < \alpha_1 < .4)$

2. f_1 is a measure of the gradient of the shear flow field. If δ is a characteristic thickness of the shear flow layer, then $f_1 \sim a/\delta$.

3. f_2 is proportional to the length of the integration region. The thickness of the shear layer is a measure of the length over which the target material is softening. Then $f_2 \sim \delta/a$.

Thus, for the purpose of constructing an approximate theory, we assume α is a constant.

Using α which we assume to be constant, we substitute $\langle\sigma_F\rangle$ of Eq. (45) for σ_F of Eq. (35), obtaining:

$$E_{*p} = C_2\alpha C_p T_m \ln\left(\frac{\sigma_F(T_1,\dot{\varepsilon})}{\alpha\rho C_p T_m} + 1\right) \qquad (47)$$

Correlating this theoretical result with the data from our impact experiments, we arrive at values for the constants α and C_2. In this equation at the current time we use:

$$\alpha = 0.05$$
$$C_2 = 6.64$$

We have found that this formula predicts E_{*p} for a wide variety of materials to about $\pm$ 16%.

In figure 30 the experimental value of E_{*p} is compared to the theoretical result from Eq. (47). The solid squares plot the ratio of experimental to theoretical E_{*p} for materials as dissimilar as Lexan, steel, and lead. All the points fall within the error band of $\pm$ 16%. As a means of comparison, the open circles plot the ratio of experimental E_{*p} to the heat of fusion H_f of the target material. H_f has sometimes been used as an indicator of E_{*p}. One sees in figure 30 that H_f works well for some materials but not for lead, copper or aluminum. In addition, there is no H_f for Lexan. In comparison, our formula, Eq. (47), predicts accurately the E_{*p} for all these materials as well as others presented in this report.

The total E_* of a target material is the sum of the plastic part and the elastic part:

$$E_{*t} = E_{*e} + E_{*p} \qquad (48)$$

E_{*p} is a constant vs. p/d, while $E_{*e} \sim (p/d)^{-.75}$. For most of the materials, particularly the pure metals presented in Chapter 3, the elastic contribution is quite small, so E_{*t} is almost constant with p/d. A typical example of this is zinc, shown in figure 31. Just the reverse holds true for Lexan, figure 28, where $E_{*e} > E_{*p}$ for $p/d < 2$.

For the entire range of materials tested, the results of which were presented in Chapter 3, the theoretical predictions obtained from E_{*t} were found to be in good agreement with the data over a wide range of p/d.

The true test of a theory is whether it can accurately predict the outcome of an experiment <u>in advance</u> of the experiment. In figures 32, 33, and 34 we present predictions for three

EXPERIMENT vs. THEORY FOR E_{*p}

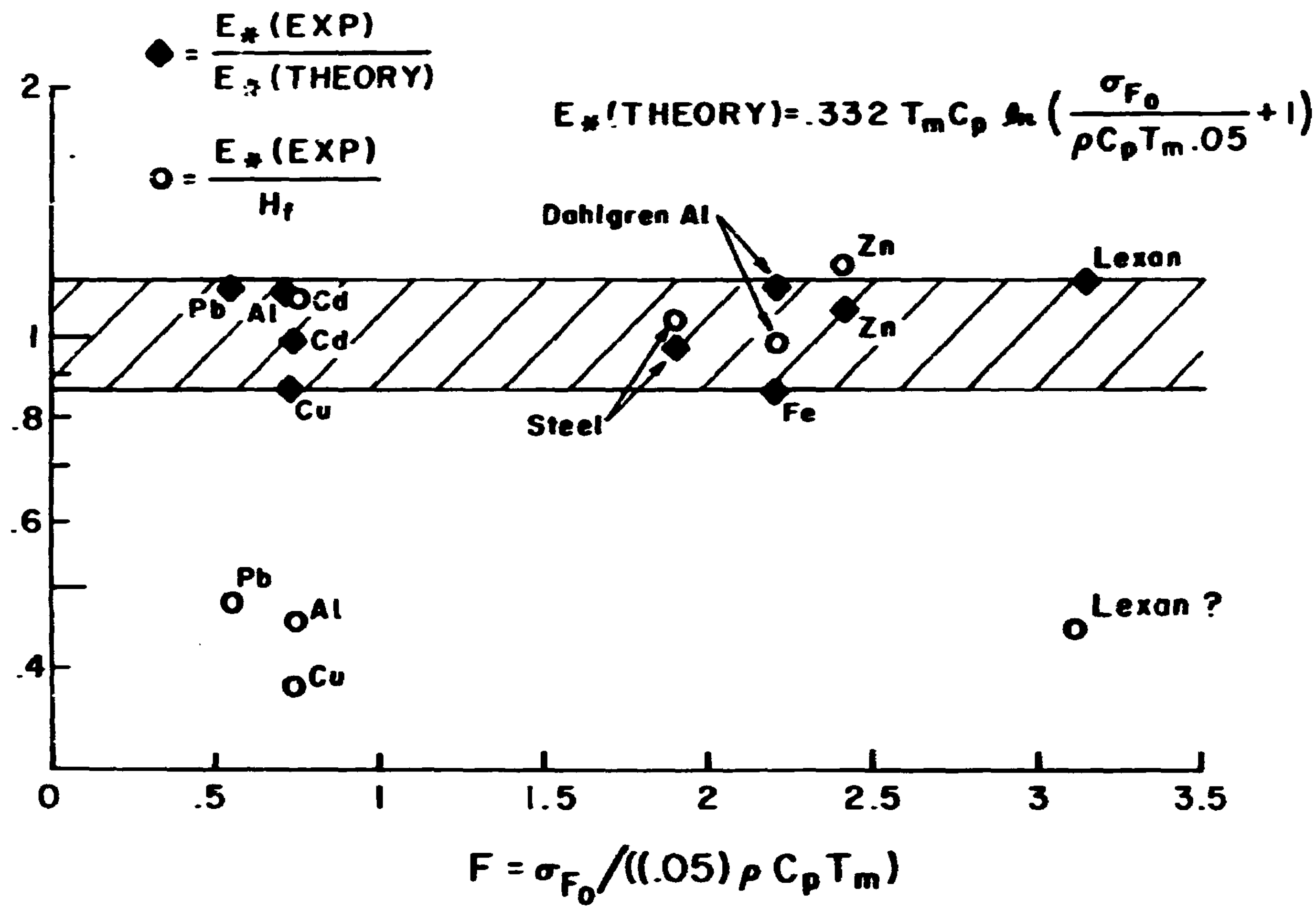

Figure 30

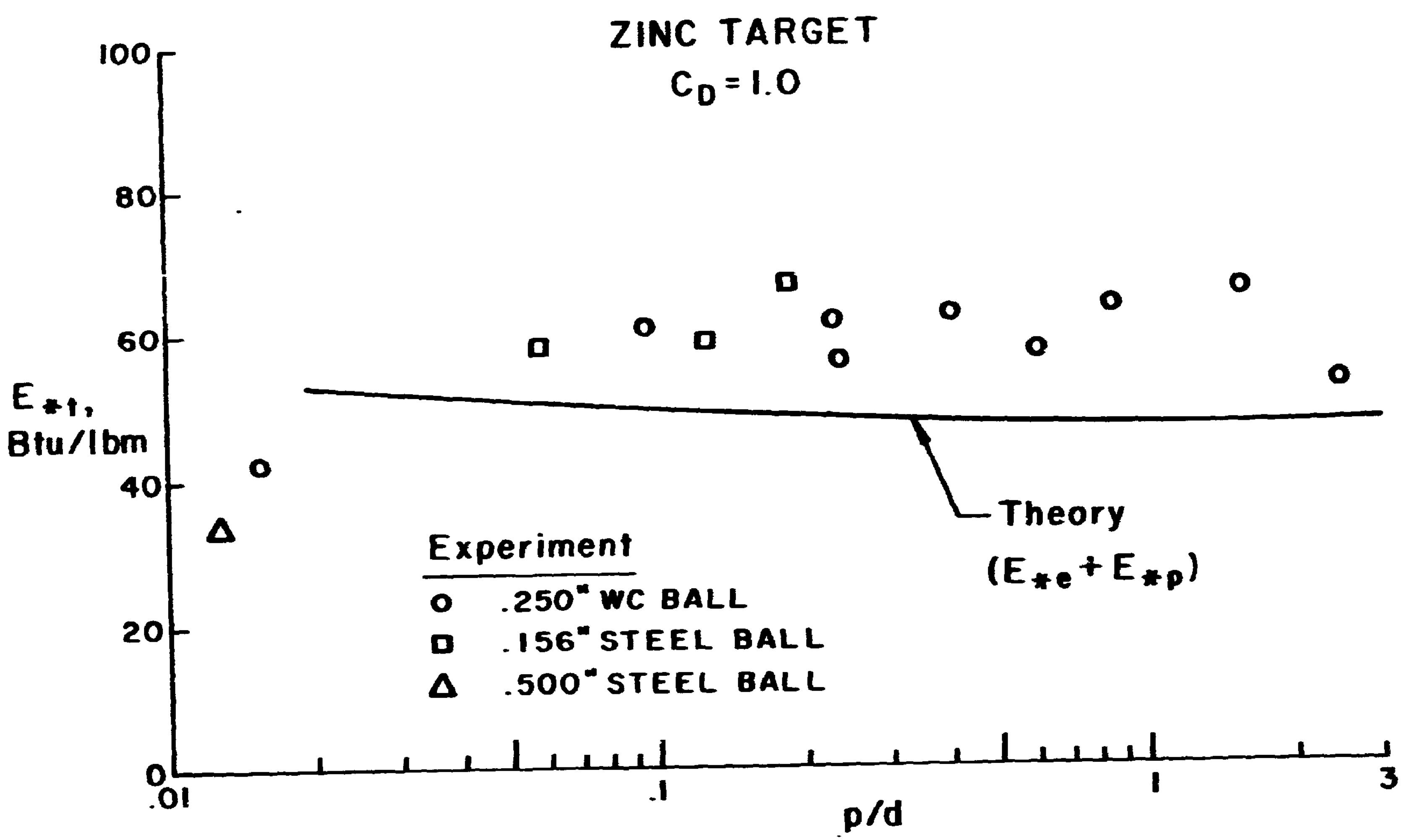
ZINC TARGET
$C_D = 1.0$
E_{*t}, Btu/lbm
100
80
60
40
20
0
.01
.1
1
3
p/d
Theory
$(E_{*e} + E_{*p})$
Experiment
.250" WC BALL
.156" STEEL BALL
.500" STEEL BALL

Figure 31

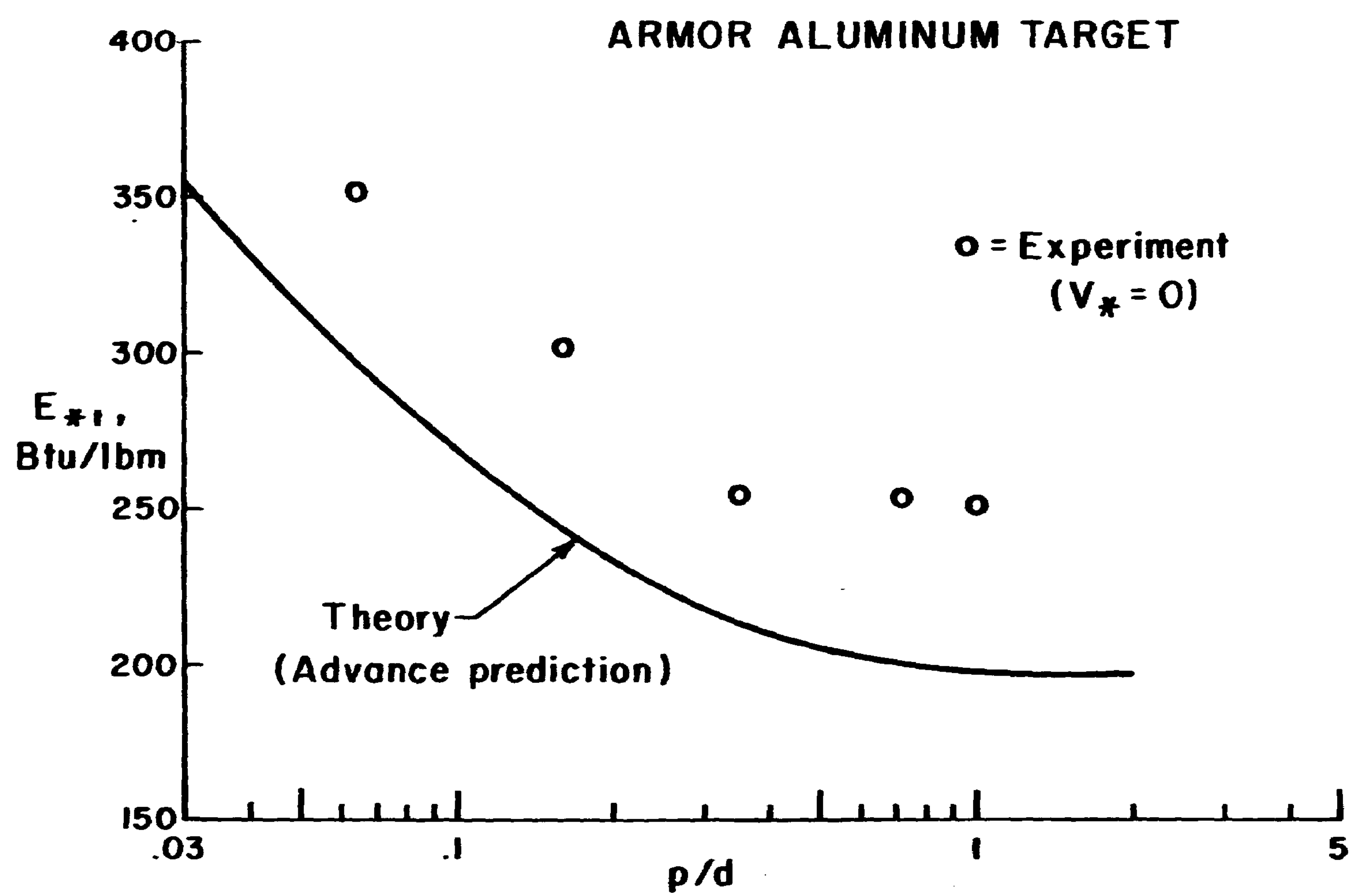
ARMOR ALUMINUM TARGET
o = Experiment
($V_* = 0$)
E_{*1},
Btu/lbm
400
350
300
250
200
150
.03
.1
1
5
p/d
Theory
(Advance prediction)

Figure 32

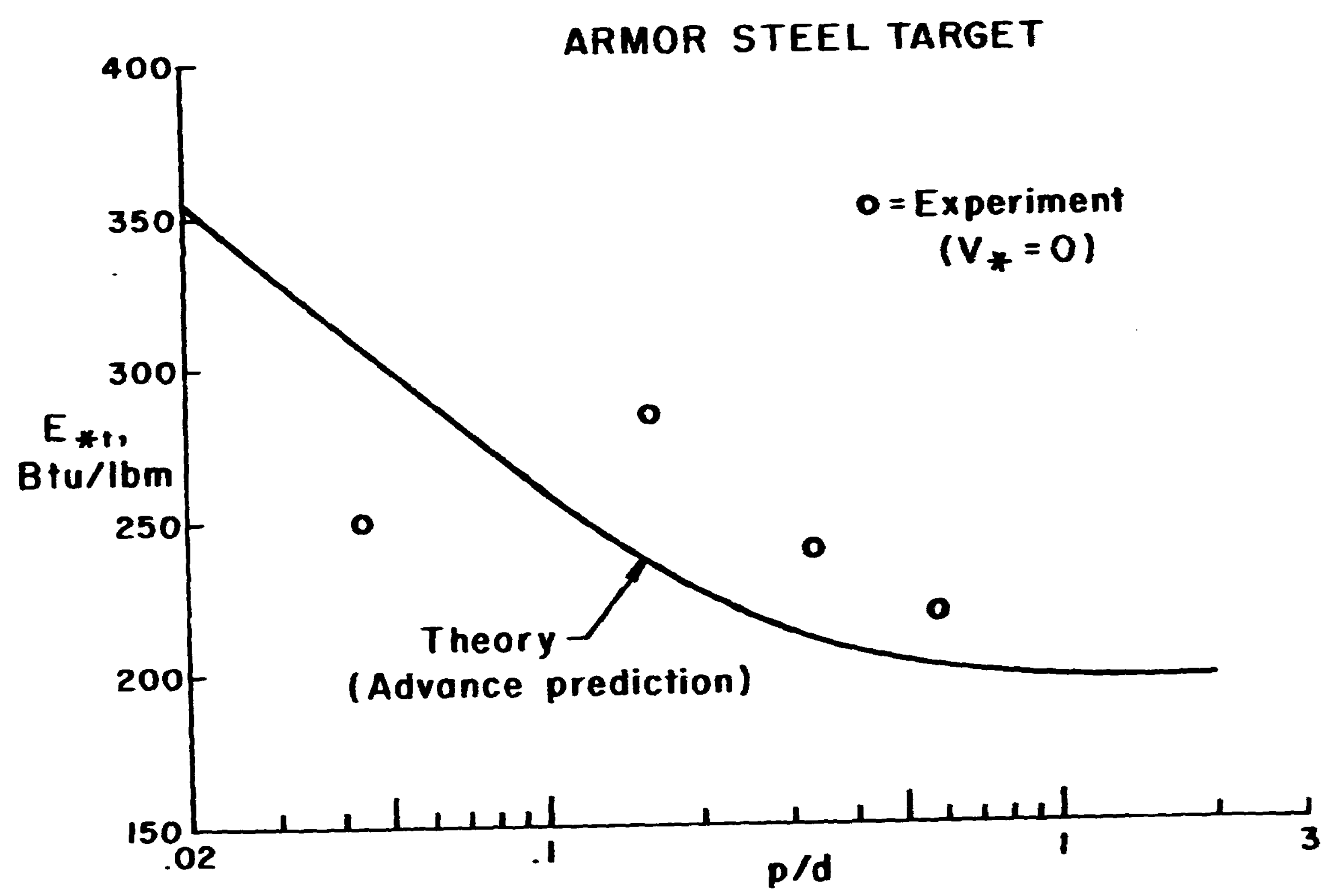
ARMOR STEEL TARGET
o = Experiment
($V_* = 0$)
Theory
(Advance prediction)
E_{*t},
Btu/lbm
400
350
300
250
200
150
.02
.1
1
3
p/d

Figure 33

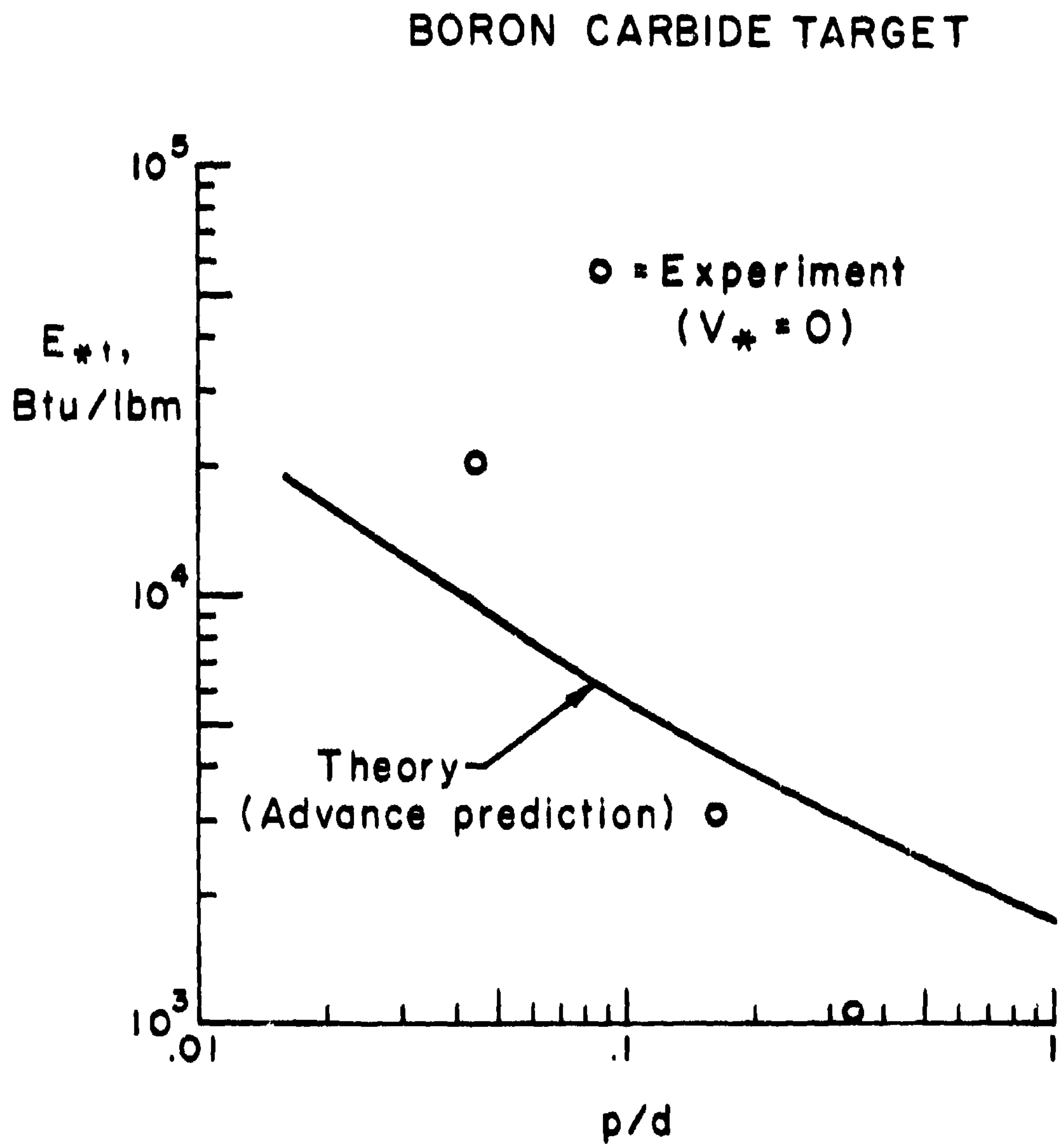

BORON CARBIDE TARGET
o = Experiment
($V_* = 0$)
E_{*t},
Btu/lbm
10^5
10^4
10^3
Theory
(Advance prediction)
.01
.1
1
p/d

Figure 34

different materials made several weeks before the impact tests were carried out. Figure 32 presents the prediction and experimental data for armor aluminum. The data clearly show the predicted elastic behavior at low p/d as well as the asymptotic approach to E_{*p} for large p/d . The overall agreement between experiment and theory is within better than 20%. In figure 33 is presented the data for armor steel and the theoretical curve, also predicted in advance of experiment. Again, the elastic region is discernible, and the overall agreement with theory is 15% or better.

A test of great interest to us was that of boron carbide, B_4C , since our theory for E_* predicts that all the light, hard ceramics, particularly B_4C , should have very high E_*'s , many times that of armor steel or armor aluminum. Our prediction of E_{*p} for B_4C is 1197 BTU/lbm, compared to around 200 BTU/lbm for steel and aluminum armor. In addition, the elastic contribution is large at low p/d . Using the published value of hardness of 2800 kg/mm² , published values of E , ρ , T , and C_p , we obtained from our formulas the prediction plotted as a solid line in figure 34. Our first three data points, which were obtained afterward, are also plotted. Note the vertical axis is logarithmic with values of 10,000 BTU/lbm obtained at low p/d , and approaching 1,000 BTU/lbm at p/d = 4 . Because the targets we used were ~ .4" thick, backface effects became important at larger p/d , quite possibly reducing the experimental value of E_* . Thicker targets and higher velocity experiments are required to check our theory at deeper penetration. Nevertheless, it is clear that our theory is rather successful in predicting the extremely good armor properties of boron carbide.

Thus, we believe we understand the mechanisms involved in armor and we have derived a theory which is good at the extremes of very soft materials (lead) to very hard materials (B_4C), from very elastic materials (Lexan), to very inelastic materials (zinc). For lightweight armor what is required is a high E_* . Using the formula of Eq. (47) for E_{*p} we have compiled a table of 69 materials for which hardness data and other parameters could be obtained, presented in Appendix I. From this we summarize in Table 3 those materials with the highest E_{*p}, which should therefore make the best lightweight armor.

On the list appear a number of materials which, it is known, are good armor materials, such as Be_2C , B_4C , BeO , TiB_2 , Al_2O_3 etc. Silicon, hard chromium and other materials are included at the end of the table for comparison.

The ranking presented here is based on E_* alone, which assumes no deformation of the penetrator. If this is included, the pressure developed at the front face of the penetrator also becomes a consideration. One wants the highest practical pressure at the leading face in order to plastically deform the penetrator. For low velocities the pressure is just $\rho_t E_{*p}$. Thus, for a given E_{*p} , one desires the armor with the highest density. For example, TiB_2 , although it has an E_{*p} 20% lower than B_4C ,

has 78% higher density and may make a better armor because it deforms the penetrator more. A program is currently underway to include in the above analysis the effects of deforming penetrators.

TABLE 3

PROMISING ARMOR MATERIALS

Material	$E_{*P}\left(\frac{Btu}{lbm}\right)$	BHN	Material	$E_{*P}\left(\frac{Btu}{lbm}\right)$	BHN
C (Diamond)	1396	8000	B_3Si	756	2200
B	1287	2800	Al_2O_3	755	2100
Be_2C	1241	1300	BP	740	3000
B_4C	1197	2800	MgO	734	800
AlB_{12}	1152	2500	VC	703	2800
BeO	1123	1300	VB_2	691	2000
ScB_4	1097	3400	Si_3N_4	661	2800
B_3Si	1041	3000	VN	615	2800
ZrB_{12}	1002	2300	Si	407	820
TiB_2	951	3000	Cr (hard)	320	1000
TiN	839	2800	W_2C	226	3500
ScB_2	800	1500	Al (armor)	196	135
SiC	800	2400	Steel (armor)	193	300
TiC	776	2400	Steel (mild)	139	164

CHAPTER 5

Conclusions

A wide range of target materials has been tested in the A.R.A.P. Impact Facility and their impact properties have been evaluated using the integral theory of impact. The results demonstrate that good correlation can be achieved between theory and data using the two characteristic material properties E_* and V_* (or, alternatively, E_{*p} and E_{*e}).

A theory has been developed which relates these two parameters to more fundamental material properties. The agreement between theory and the experimentally deduced value of E_* and V_* is very good. The theory predicts a plastic contribution to E_* which is roughly constant for a given material and an elastic contribution which is a function of the depth of penetration. The elastic contribution is small for most metals but for some materials such as polycarbonate, it is the dominant effect for small penetrations.

The results demonstrate that for present day armors E_* is typically 200 BTU/lbm. The theory suggests many candidate armor materials with vastly superior E_* capability. One of these materials, boron carbide, has been tested and a value of $E_* = 1200$ BTU/lbm has been obtained - a value in good agreement with the theory.

It is now possible to utilize the knowledge obtained in this program to optimize the design of armor (or penetrator) systems. This is the object of the next portion of the program.

REFERENCES

1. Donaldson, Coleman duP. and McDonough, Thomas B.: A Simple Integral Theory for Impact Cratering by High Speed Particles. DNA 3234F, Aeronautical Research Associates of Princeton, Inc., Princeton, NJ 08540, 4 December 1973.

2. Donaldson, Coleman duP., Contiliano, Ross M., and McDonough, Thomas B.: A Study of Water Drop Displacement and Deformation in Aerodynamic Shock Layers. A.R.A.P. Rept. No. 265, Aeronautical Research Associates of Princeton, Inc., January 1976.

APPENDIX I

THEORETICAL E_{*p} FOR ASSORTED MATERIALS

	$C_p\left(\frac{J}{kg^\circ K}\right)$	$T_m(^\circ K)$	$B\left(\frac{kg}{mm^2}\right)$	$\rho\left(\frac{kg}{m^3}\right)$	$E_{*p}\left(\frac{BTU}{lbm}\right)$	Material
1	0.554000E 03	0.297300E 04	0.240000E 04	0.321000E 04	0.752591E 03	SiC
2	0.837000E 03	0.199000E 04	0.110000E 04	0.260000E 04	0.665291E 03	SiO_2 (quartz)
3	0.522000E 03	0.168300E 04	0.165000E 03	0.233000E 04	0.222509E 03	Si (porous)
4	0.522000E 03	0.168300E 04	0.820000E 03	0.233000E 04	0.407560E 03	Si (fused)
5	0.877000E 03	0.107400E 04	0.360000E 02	0.216000E 04	0.696650E 02	NaCl
6	0.955000E 03	0.262300E 04	0.280000E 04	0.252000E 04	0.115742E 04	B_4C
7	0.134900E 04	0.260000E 04	0.150000E 04	0.301000E 04	0.112560E 04	BeO
8	0.770000E 03	0.231800E 04	0.210000E 04	0.396000E 04	0.755029E 03	Al_2O_3 (crystal)
9	0.770000E 03	0.231800E 04	0.100000E 04	0.396000E 04	0.575559E 03	Al_2O_3 (sintered)
10	0.138500E 04	0.240000E 04	0.130000E 04	0.190000E 04	0.124685E 04	Be_2C
11	0.138000E 03	0.366300E 04	0.260000E 03	0.193000E 05	0.766112E 02	W
12	0.563000E 03	0.341300E 04	0.240000E 04	0.493000E 04	0.776855E 03	TiC
13	0.936000E 03	0.933000E 03	0.125000E 03	0.270000E 04	0.165035E 03	Al (armor)
14	0.973000E 03	0.307300E 04	0.800000E 03	0.358000E 04	0.754870E 03	MgO
15	0.628000E 03	0.380000E 04	0.860000E 04	0.351000E 04	0.135077E 04	C (diamond)
16	0.709000E 03	0.317300E 04	0.300000E 04	0.450000E 04	0.956652E 03	TiB_2
17	0.180000E 03	0.416300E 04	0.275000E 04	0.122000E 05	0.516246E 03	H_fC
18	0.188000E 03	0.415300E 04	0.200000E 04	0.139600E 05	0.279602E 03	TaC
19	0.431000E 03	0.317300E 04	0.190000E 04	0.697000E 04	0.505137E 03	NbB_2

APPENDIX I (cont.)

	$C_p\left(\frac{J}{kg\,^\circ K}\right)$	$T_m(^\circ K)$	$B\left(\frac{kg}{mm^2}\right)$	$\rho\left(\frac{kg}{m^3}\right)$	$E_{sp}\left(\frac{BTU}{lbm}\right)$	Material
20	0.661000E 03	0.267300E 04	0.200000E 04	0.510000E 04	0.691196E 03	VB_2
21	0.327000E 03	0.377300E 04	0.300000E 04	0.750000E 04	0.554552E 03	NbC
22	0.521000E 03	0.182300E 04	0.280000E 04	0.700000E 04	0.447205E 03	$Cr_{23}C_6$
23	0.161000E 03	0.300[illegible]00E 04	0.350000E 04	0.175000E 05	0.226451E 03	W_2C
24	0.598000E 03	0.347000E 04	0.260000E 04	0.522000E 04	0.855942E 03	TiN
25	0.547000E 03	0.259000E 04	0.280000E 04	0.613000E 04	0.615079E 03	VN
26	0.517000E 03	0.195000E 04	0.240000E 04	0.570000E 04	0.475526E 03	Cr_2Si
27	0.104600E 04	0.257300E 04	0.280000E 04	0.234000E 04	0.126753E 04	B
28	0.736000E 03	0.295300E 04	0.230000E 04	0.270000E 04	0.106160E 04	ZrB_{12}
29	0.804000E 03	0.250000E 04	0.360000E 04	0.252000E 04	0.104161E 04	B_3Si
30	0.811000E 03	0.152300E 04	0.300000E 04	0.250000E 04	0.746465E 03	BP
31	0.84[illegible]000E 03	0.170000E 04	0.220000E 04	0.240000E 04	0.725745E 03	B_3Si
32	0.598000E 03	0.180000E 04	0.250000E 04	0.545000E 04	0.375050E 03	YbB_6
33	0.574000E 03	0.320000E 04	0.30[illegible]E 04	0.670000E 04	0.545992E 03	ZrB
34	0.246900E 03	0.330000E 04	0.250000E 04	0.105000E 05	0.342025E 03	HfB_2
35	0.196000E 03	0.270300E 04	0.250000E 04	0.140000E 05	0.234084E 03	TaB
36	0.212000E 03	0.292300E 04	0.250000E 04	0.155000E 05	0.262625E 03	Ta_3B_4
37	0.196000E 03	0.320000E 04	0.240000E 04	0.160000E 05	0.246924E 03	WB
38	0.103700E 04	0.242300E 04	0.250000E 04	0.258000E 04	0.113257E 04	AlB_{12}
39	0.816000E 03	0.250000E 04	0.340000E 04	0.244000E 04	0.109785E 04	ScB_4
40	0.459000E 03	0.240000E 04	0.240000E 04	0.485000E 04	0.528515E 03	PrB_6

APPENDIX I (cont.)

	$C_p\left(\frac{J}{kg^{\circ}K}\right)$	$T_m(^{\circ}K)$	$B\left(\frac{kg}{mm^2}\right)$	$\rho\left(\frac{kg}{m^3}\right)$	$E_{sp}\left(\frac{BTU}{lbm}\right)$	Material
41	0.560000E 03	0.220000E 04	0.200000E 04	0.553000E 04	0.495066E 03	Cr_3B_2
42	0.176000E 03	0.314500E 04	0.160000E 04	0.156350E 05	0.196093E 03	WC
43	0.182500E 03	0.363300E 04	0.160000E 04	0.154600E 05	0.255827E 03	TaN
44	0.565000E 03	0.220000E 04	0.280000E 04	0.344000E 04	0.661592E 03	Si_3N_4
45	0.885000E 03	0.252000E 04	0.150000E 04	0.365000E 04	0.800046E 03	ScB_2
46	0.617000E 03	0.252500E 04	0.120000E 04	0.528000E 04	0.511594E 03	VB
47	0.333000E 03	0.380000E 04	0.260000E 04	0.590000E 04	0.335674E 03	ZrC
48	0.172000E 03	0.305000E 04	0.220000E 04	0.170000E 05	0.206716E 03	W_2B
49	0.840000E 03	0.395200E 04	0.195000E 02	0.225000E 04	0.701704E 02	C (graphite)
50	0.161000E 04	0.550000E 03	0.500000E 02	0.141000E 04	0.199920E 03	Kevlar - 49
51	0.117000E 04	0.325000E 03	0.200000E 02	0.120600E 04	0.124005E 03	Lexan
52	0.459000E 03	0.160500E 04	0.164000E 03	0.750000E 04	0.135362E 03	Steel (mild)
53	0.459000E 03	0.160900E 04	0.300000E 03	0.750000E 04	0.193246E 03	Steel (armor)
54	0.459000E 03	0.160900E 04	0.190000E 03	0.750000E 04	0.136261E 03	Fe (cast iron)
55	0.384000E 03	0.135600E 04	0.510000E 02	0.590000E 04	0.406555E 02	Cu
56	0.547000E 03	0.593000E 03	0.178000E 02	0.354000E 04	0.259225E 02	Cd
57	0.382000E 03	0.692000E 03	0.380000E 02	0.700000E 04	0.465505E 02	Zn
58	0.125000E 03	0.600000E 03	0.450000E 01	0.113400E 05	0.397706E 01	Pb
59	0.936000E 03	0.933000E 03	0.135000E 03	0.270000E 04	0.196426E 03	Al (armor)
60	0.936000E 03	0.933000E 03	0.260000E 02	0.270000E 04	0.687427E 02	Al (pure)
61	0.299000E 03	0.296000E 04	0.200000E 04	0.890000E 04	0.355509E 03	Mo_2C

APPENDIX I (concluded)

	$C_p\left(\frac{J}{kg^oK}\right)$	$T_m(^oK)$	$B\left(\frac{kg}{mm}\right)$	$\rho\left(\frac{kg}{m}\right)$	$E_{sp}\left(\frac{BTU}{lbm}\right)$	Material
62	0.177000E 03	0.415300E 04	0.180000E 04	0.159000E 05	0.255548E 03	TaC
63	0.460000E 03	0.214800E 04	0.160000E 04	0.719000E 04	0.326077E 03	Cr (hard)
64	0.129000E 03	0.297300E 04	0.350000E 03	0.129000E 06	0.196887E 02	Os
65	0.544000E 03	0.308300E 04	0.260000E 04	0.577000E 04	0.705420E 03	VC
66	0.276000E 03	0.288300E 04	0.160000E 03	0.102200E 05	0.107115E 03	Mo
67	0.266000E 03	0.332300E 04	0.900000E 03	0.986000E 04	0.251773E 03	ThO_2
68	0.753000E 03	0.211600E 04	0.850000E 03	0.426000E 04	0.491536E 03	TiO_2
69	0.519000E 03	0.194100E 04	0.374000E 03	0.450000E 04	0.259403E 03	Ti